THE UNIVERSITY *of* EDINBURGH

Edinburgh Research Explorer

Near-inertial scattering by random flows

OPEN ACCESS

Near-inertial wave scattering by random flows

Eric Danioux and Jacques Vanneste*

School of Mathematics and Maxwell Institute for Mathematical Sciences,

University of Edinburgh, Edinburgh EH9 3JZ, UK

Abstract

The impact of a turbulent flow on wind-driven oceanic near-inertial waves is examined using a linearised shallow-water model of the mixed layer. Modelling the flow as a homogeneous and stationary random process with spatial scales comparable to the wavelengths, we derive a transport (or kinetic) equation governing wave-energy transfers in both physical and spectral spaces. This equation describes the scattering of the waves by the flow which results in a redistribution of energy between waves with the same frequency (or, equivalently, with the same wavenumber) and, for isotropic flows, in the isotropisation of the wave field. The time scales for the scattering and isotropisation are obtained explicitly and found to be of the order of tens of days for typical oceanic parameters. The predictions inferred from the transport equation are confirmed by a series of numerical simulations.

Two situations in which near-inertial waves are strongly influenced by flow scattering are investigated through dedicated nonlinear shallow-water simulations. In the first, a wavepacket propagating equatorwards as a result from the β-effect is shown to be slowed down and dispersed both zonally and meridionally by scattering. In the second, waves generated by moving cyclones are shown to be strongly disturbed by scattering, leading again to an increased dispersion.

arXiv:1601.05456v2 [physics.ao-ph] 8 Jun 2016

---

* Corresponding author: J.Vanneste@ed.ac.uk

I. INTRODUCTION

Near-inertial waves (NIWs), that is, internal waves with frequencies close to the local Coriolis frequency, are a major source of variability in the ocean where they play an important dynamical role (see [1] for a recent review of NIW observations and models). They are mainly generated at the surface by wind-stress forcing, although other generation mechanisms exist including geostrophic adjustment [2], flow-topography interaction [3], momentum deposition [4, 5], and spontaneous generation [6, 7]. Wind-generated NIWs have small vertical scales, leading to strong vertical shear, instabilities and, as a result, surface mixing. Because of this and because of the vertical motion they induce, they have a strong impact on biological production [8]. NIWs also propagate to the deep ocean [9] where they eventually dissipate and induce diapycnal mixing, potentially sustaining the meridional overturning circulation; the extent of their contribution to the latter is still a matter of debate [10]. There is also mounting evidence of a direct energetic impact of NIWs on the mesoscale flow [11–13].

Regions of NIW-generation usually coincide with regions of strong geostrophic turbulence (see for example Fig. 1 in [14]). This has motivated numerous studies of the impact of a flow on the propagation of NIWs [11, 15–21]. Because of the different atmospheric and oceanic Rossby radii, the horizontal scales of the wind patterns and hence of the NIW forcing are often much larger than scales of the oceanic flow. Consequently, many of the aforementioned studies take the NIWs as initially homogeneous. However, as shown by D'Asaro [22] and confirmed by Alford [23] and Silverthorne and Toole [24], most of the NIW energy input to the ocean is due to a few intense winter storms or cyclones, with horizontal scales of hundreds of kilometers. These storms move horizontally, exciting NIWs at scales that depend on their speed and can be comparable to oceanic scales, then invalidating the assumption of homogeneous initial condition. There is, then, a need to understand how the flow affects NIWs generated at scales comparable to flow scales. The primary effect is the scattering of the NIWs, leading to a redistribution of their energy in wavenumber space. Describing and quantifying this scattering are the aims of the present paper.

We adopt the framework developed by Ryzhik *et al.* [25] for a broad class of scattering problems (see also Ref. 26). This describes asymptotically the propagation of a spectrum of waves in a medium – the flow in our case – that varies randomly over spatial scales similar

2

to the wavelength. The approach represents the wave field by its Wigner transform to account for large-scale spatial modulations of the wave spectrum. Taking the model of NIW propagation derived by Young and Ben Jelloul [19, referred below as YBJ] as our starting point, we derive the transport equation satisfied by the associated Wigner transform and examine several predictions of this equation. The principal one is the spreading of the NIW energy spectrum along lines of constant frequency (corresponding to constant horizontal wavenumber for NIWs), leading to a relaxation towards an isotropic spectrum when the flow is itself isotropic. We estimate the timescale for this relaxation, and find it to be of the order of a few weeks, depending on parameters including the flow strength and correlation length. We test our analytic predictions against numerical simulations of a reduced-gravity shallow-water version of the YBJ model.

The importance of scattering for NIWs and the relevance of our theoretical conclusions are illustrated by two applications which we discuss on the basis of simulations of the full nonlinear reduced-gravity shallow-water model. This model introduces more realism through effects not included in the YBJ and scattering theories. The first application considers the interplay between scattering and the β-effect; it shows that this interplay leads a slowdown of the equatorward propagation of NIW wavepackets. The second application considers NIWs generated by a moving cyclone and identifies a speedup of lateral dispersion as one of the main impacts of the flow.

The plan of the paper is as follows. In section II, we briefly review various approaches to the study of NIW propagation in background flows. Section III introduces the transport equation obeyed by the Wigner function associated with NIWs. Because of its mathematical complexity, the derivation of this equation is relegated to Appendix A. Section III also shows how the isotropisation of the wave field results from the scattering, estimates the relevant timescales as a function of the flow parameters, and verifies the analytic predictions numerically. The two applications are presented in section IV. The paper concludes with a discussion in section V.

II. NIW PROPAGATION IN FLOWS

Many studies of the propagation of oceanic internal waves in heterogeneous flows rely on the Wentzel–Kramers–Brillouin (WKB) approximation [15, 16, 18] which assumes that the

length scale ℓ_w of the waves is much smaller than the scale ℓ_f of the background flow. Wind-driven NIWs, however, typically span a broad range of scales, from the large atmospheric scales at which they are generated to the much smaller scales they reach as a result of advection and refraction by the flow. To account for this, Young and Ben Jelloul [19] proposed a model for the propagation of NIWs in a geostrophic flow without any assumptions on their relative scale ℓ_w/ℓ_f. Using a multiple time-scale approach (where the slow time scale is related to the small NIW-Burger number), they derived an equation for the subinertial amplitude M from which the NIW complex velocity is deduced as $u + iv = Me^{-if_0t}$. With the additional assumption of a barotropic geostrophic flow with streamfunction $\psi(x, y, t)$, the amplitude of each vertical mode obeys the YBJ equation

$$\partial_t M + \boldsymbol{\nabla}^\perp \psi \cdot \boldsymbol{\nabla} M - i\frac{h}{2}\Delta M + i\frac{\Delta\psi}{2}M = 0, \tag{1}$$

where $h = f_0 r_n^2$ depends on the NIW-vertical mode n through its Rossby radius of deformation r_n, and $\boldsymbol{\nabla}^\perp = (-\partial_y, \partial_x)$. This equation, which holds provided that

$$\mathrm{Bu} = r_n^2/\ell_w^2 \ll 1, \tag{2}$$

exhibits the three physical mechanisms influencing the evolution of NIWs, namely advection, dispersion and refraction. It also applies to NIWs concentrated in a homogeneous layer capping an abyssal ocean where the only motion is the barotropic flow, as described by a reduced-gravity shallow-water model; in this case, $h = g'H/f_0$ where g' is the reduced gravity and H is the depth of the top layer, and $\mathrm{Bu} = g'H/(f^2\ell_w^2)$ (see [27]). This is the interpretation that we take in this paper, focussing on applications to mixed-layer NIWs.

Most of the work on (1) considers the case of homogeneous initial NIWs, that is, infinite initial ℓ_w or, more broadly, $\ell_w \gg \ell_f$ [e.g. 19, 20, 28]. Finite length scales appear as a result of the interactions with the flow, leading to a ratio ℓ_w/ℓ_f that depends on the value of h/Ψ. In the long-time limit, this ratio becomes $O(\sqrt{h/\Psi})$ in the strong dispersion regime $h \gg \Psi$, $O(1)$ in the intermediate regime $h = O(\Psi)$, and h/Ψ in the strong trapping regime $h \ll \Psi$ [27]. The opposite limit, where $\ell_w \ll \ell_f$ initially can be tackled using the WKB approximation. It is clear from (1) that the refraction term becomes much smaller than the advection term in this limit, except for some very specific flow configurations, as noted by Olbers [17].

The case where $\ell_w \sim \ell_f$ initially remains largely unexplored despite its relevance to oceanic situations (see section IV). It is the focus of this paper. We make analytical progress by

	spatial scale	time scale
wave phase	ℓ	ℓ^2/h
wave envelope	$L = \ell/\epsilon$	$L\ell/h = \epsilon L^2/h$
flow	ℓ	$L\ell/h = \epsilon L^2/h$

TABLE I. Scaling assumptions: the wave time scales are deduced from the spatial scales using the dispersion relation $\omega = h|\boldsymbol{k}|^2/2$ for the frequency shift relative to the inertial frequency f_0. The flow amplitude is determined by the scaling $\Psi = O(\epsilon^{1/2}h)$ of the streamfunction.

assuming that the NIW field consists of a spectrum of waves whose phase varies on the flow scale, thus taking $\ell_{\mathrm{w}} = \ell_{\mathrm{f}} =: \ell$ from now on. Inhomogeneities in the wave field are accounted for by considering an amplitude that varies on a much larger length scale $L = \ell/\epsilon$, where $\epsilon \ll 1$. The flow is taken to be relatively weak, specifically such that $\Psi/h = O(\epsilon^{1/2})$, and modelled by a homogeneous and stationary random process in space and time. The scaling assumptions are further discussed in Appendix A and summarised in Table I. We next derive the transport equation that governs the dynamics of the wave field in this setup.

III.   NIW SCATTERING

We adopt the approach of Ryzhik *et al.* [25], formulated in terms of the Wigner transform which we now introduce.

A.   Wigner transform

The Wigner transform of a function $M(\boldsymbol{x}, t)$ rapidly decaying at infinity is defined as

$$W(\boldsymbol{x}, \boldsymbol{k}, t) = \frac{1}{4\pi^2} \int_{\mathbb{R}^2} \mathrm{e}^{\mathrm{i}\boldsymbol{k}\cdot\boldsymbol{y}} M(\boldsymbol{x} - \boldsymbol{y}/2, t) M^*(\boldsymbol{x} + \boldsymbol{y}/2, t) \, \mathrm{d}\boldsymbol{y}, \tag{3}$$

where * denotes the complex conjugate. Here, both $\boldsymbol{x}$ and $\boldsymbol{k}$ are two-dimensional (horizontal) vectors. It is easy to show that $W(\boldsymbol{x}, \boldsymbol{k}, t)$ is real and that its integral over wavevector space is

$$\int_{\mathbb{R}^2} W(\boldsymbol{x}, \boldsymbol{k}, t) \, \mathrm{d}\boldsymbol{k} = |M(\boldsymbol{x}, t)|^2. \tag{4}$$

In the context of the YBJ equation, this quantity is twice the local NIW kinetic energy. For a wavepacket solution

$$M(\boldsymbol{x}, t) = A(\boldsymbol{x}, t)\mathrm{e}^{\mathrm{i}\boldsymbol{k}_0\cdot\boldsymbol{x}/\epsilon}, \tag{5}$$

where A is a smooth function of $\boldsymbol{x}$ and $|\boldsymbol{k}_0| = O(1)$, the Wigner transform tends to

$$W(\boldsymbol{x}, \boldsymbol{k}, t) \to |A(\boldsymbol{x}, t)|^2 \delta(\boldsymbol{k} - \boldsymbol{k}_0/\epsilon)$$

as the scale-separation parameter $\epsilon \to 0$. Hence, the Wigner transform can be intuitively thought of as a wavenumber-resolving energy density in the scale-separation regime, and therefore bears similarities with wavelet transforms.

B. Transport equation

We assume that the NIW field consists of a spectrum of wavepackets of the form (5), with phases that vary on the flow scale and amplitudes that vary on a much larger scale. In other words, the waves fluctuate on the flow scale, but are modulated over a larger envelope scale, with the scale separation measured by $\epsilon \ll 1$. This assumption implies that the scaled Wigner transform

$$W^\epsilon(\boldsymbol{x}, \boldsymbol{k}, t) = \epsilon^{-2}W(\boldsymbol{x}, \boldsymbol{k}/\epsilon, t), \tag{6}$$

where $\boldsymbol{x}$ and $\boldsymbol{k}$ are non-dimensionalised using the large envelope scale $L = \epsilon^{-1}\ell$, tends to a finite limit W^0 as $\epsilon \to 0$. The flow, represented by a random streamfunction $\psi(\boldsymbol{x}, t)$ with stationary and homogeneous statistics, has an amplitude Ψ that satisfies the scaling $\Psi/h = O(\epsilon^{1/2})$ (see Appendix A). This ensures that effects associated with the flow are smaller than dispersion effects in Eq. (1). In stronger flows, waves simply do not propagate while weaker flows do not affect wave propagation on realistic timescales.

Under these assumptions, the leading-order Wigner transform W^0 of M, denoted below simply by W, satisfies the transport equation

$$\partial_t W + h\boldsymbol{k} \cdot \boldsymbol{\nabla}_{\boldsymbol{x}} W = \mathcal{L}W - \Sigma(\boldsymbol{k})W, \tag{7}$$

where

$$\mathcal{L}W = \int_{\mathbb{R}^2} \sigma(\boldsymbol{k}, \boldsymbol{p})W(\boldsymbol{x}, \boldsymbol{p}, t)\, \mathrm{d}\boldsymbol{p} \tag{8}$$

and

$$\Sigma(\boldsymbol{k}) = \int_{\mathbb{R}^2} \sigma(\boldsymbol{k}, \boldsymbol{p})\, \mathrm{d}\boldsymbol{p} \tag{9}$$

(see Appendix A for the derivation). Here,

$$\sigma(\boldsymbol{k}, \boldsymbol{p}) = \frac{4\pi}{h} \left(|\boldsymbol{k} \times \boldsymbol{p}|^2 + \frac{|\boldsymbol{k} - \boldsymbol{p}|^4}{4} \right) \hat{R}(\boldsymbol{p} - \boldsymbol{k}) \delta(\boldsymbol{k}^2 - \boldsymbol{p}^2), \tag{10}$$

where $\hat{R}(\boldsymbol{p})$ is the power spectrum of the streamfunction (that is, the Fourier transform of its covariance, see (A14)). It is independent of time because of the assumed stationarity of the flow. Under the additional assumption of isotropy, which we will make, it depends only on the magnitude $|\boldsymbol{p}|$ of $\boldsymbol{p}$.

The function $\sigma(\boldsymbol{k}, \boldsymbol{p})$ is interpreted as a differential scattering cross-section, representing the rate at which energy at wavevector $\boldsymbol{p}$ is converted to energy at wavevector $\boldsymbol{k}$. In general, it is a function of space and time but this dependence drops here because of the homogeneity and stationarity of the flow. The total scattering cross-section $\Sigma(\boldsymbol{k})$ represents the rate at which energy at wavevector $\boldsymbol{k}$ is transferred to all other wavevectors. Importantly, the particular form of (10) shows that energy transfers are restricted to wavevectors with the same magnitude:

$$\sigma(\boldsymbol{k}, \boldsymbol{p}) = 0 \quad \text{if} \quad |\boldsymbol{k}| \neq |\boldsymbol{p}|. \tag{11}$$

This is the particularisation to NIWs, with dispersion relation $\omega(\boldsymbol{k}) = h|\boldsymbol{k}|^2/2$ (see (1)), of the general restriction of energy transfers between waves of equal frequencies: $\omega(\boldsymbol{k}) = \omega(\boldsymbol{p})$. The two terms in (10) stem from the advection and refraction terms, respectively. Wave propagation is governed by the second term on the left-hand side of equation (7), which can be identified as advection by the group velocity $\nabla_{\boldsymbol{k}} \omega(\boldsymbol{k}) = h\boldsymbol{k}$ in a WKB context.

Integration of (7) with respect to $\boldsymbol{k}$ and use of (4) and of the property $\sigma(\boldsymbol{k}, \boldsymbol{p}) = \sigma(\boldsymbol{p}, \boldsymbol{k})$ give the leading-order energy conservation equation

$$\partial_t \frac{1}{2} |M|^2 + \boldsymbol{\nabla}_{\boldsymbol{x}} \cdot \mathbf{F} = 0, \tag{12}$$

where

$$\mathbf{F} = \frac{h}{2} \int_{\mathbb{R}^2} \boldsymbol{k} W(\boldsymbol{x}, \boldsymbol{k}) \, \mathrm{d}\boldsymbol{k} = \frac{ih}{4} (M \boldsymbol{\nabla}_{\boldsymbol{x}} M^* - M^* \boldsymbol{\nabla}_x M)$$

is the NIW kinetic energy flux [19, 27].

C. Isotropisation

1. General properties

In view of (11), it is convenient to use polar coordinates for the wavevector. This simplifies (8) into the single integral

$$\mathcal{L}W(\boldsymbol{x}, |\boldsymbol{k}|, \theta, t) = \int_{-\pi}^{\pi} \sigma'(|\boldsymbol{k}|, \theta') W(\boldsymbol{x}, |\boldsymbol{k}|, \theta + \theta', t) \, \mathrm{d}\theta', \tag{13}$$

where θ is the orientation of $\boldsymbol{k}$, θ' is the angle between $\boldsymbol{k}$ and $\boldsymbol{p}$ in (8), and the differential scattering cross-section σ' is defined from (10) as

$$\sigma'(|\boldsymbol{k}|, \theta') = \frac{8\pi|\boldsymbol{k}|^4}{h} \sin^2(\theta'/2) \hat{R} \left(2|\sin(\theta'/2)\boldsymbol{k}|\right), \tag{14}$$

independent of the direction of $\boldsymbol{k}$: the scattering is rotationally invariant because the flow is isotropic. Similarly, the total scattering cross-section (9) becomes

$$\Sigma(|\boldsymbol{k}|) = \int_{-\pi}^{\pi} \sigma'(|\boldsymbol{k}|, \theta) \, \mathrm{d}\theta. \tag{15}$$

We now restrict our attention to horizontally homogeneous Wigner transforms, that is, NIWs whose large-scale properties are homogeneous. The group velocity term in (7) vanishes and the equation for W reduces to

$$\partial_t W = \mathcal{L}W - \Sigma(|\boldsymbol{k}|) W. \tag{16}$$

The solution of (16) can be calculated explicitly from the knowledge of the initial condition

$$W(|\boldsymbol{k}|, \theta, t = 0) = W_0(|\boldsymbol{k}|, \theta) \tag{17}$$

and the eigenvalues and eigenvectors of the operator $\mathcal{L}$. To find these, we remark that, from the symmetry property $\sigma'(|\boldsymbol{k}|, \theta) = \sigma'(|\boldsymbol{k}|, -\theta)$, (13) can be viewed as a convolution of σ' and W. Because the Fourier transform of a convolution is proportional to the product of the Fourier transforms of the convolved functions, the eigenvalues and eigenvectors of $\mathcal{L}$ are

$$\{\lambda_n, \cos(n\theta)\}, \ n = 0, 1, \cdots, \tag{18}$$

where

$$\lambda_n = \int_{-\pi}^{\pi} \sigma'(|\boldsymbol{k}|, \theta) \cos(n\theta) \, \mathrm{d}\theta \tag{19}$$

8

is proportional to the Fourier transform of σ' with respect to θ and depends on $|\boldsymbol{k}|$. Since σ' is non-negative and smooth,

$$\lambda_0 = \Sigma(|\boldsymbol{k}|) \quad \text{and} \quad |\lambda_{n \geq 1}| < \lambda_0. \tag{20}$$

Expanding the initial condition (17) in the basis of eigenfunctions given in (18), we write

$$W_0(|\boldsymbol{k}|, \theta) = \sum_{n=0}^{\infty} w_n(|\boldsymbol{k}|) \cos(n\theta),$$

and obtain the exact solution of (16) as

$$W(|\boldsymbol{k}|, \theta, t) = \sum_{n=0}^{\infty} w_n(|\boldsymbol{k}|) e^{(\lambda_n - \Sigma)t} \cos(n\theta). \tag{21}$$

From (20) and (21), we conclude that, regardless of the initial conditions, the solution of (16) converges, at a given wavenumber $|\boldsymbol{k}|$, to the stationary, isotropic solution given by

$$W(|\boldsymbol{k}|, \theta, t = \infty) = w_0(|\boldsymbol{k}|) = \frac{1}{2\pi} \int_{-\pi}^{\pi} W(|\boldsymbol{k}|, \theta, t = 0) \, \mathrm{d}\theta. \tag{22}$$

This is a key conclusion drawn from the transport equation: the scattering of NIWs by a random flow leads to an isotropic wave field. Moreover, the convergence timescale is deduced from (21) to be approximately

$$T \simeq 1/(\Sigma - \lambda'), \quad \text{where} \quad \lambda' = \max_{n \geq 1} \lambda_n. \tag{23}$$

We note that the scattering time Σ^{-1}, which estimates the time scale over which scattering is significant, does not necessarily provide a reliable order of magnitude for the time scale of isotropisation (23) which can be much longer. This is demonstrated in section III C 3 below.

2. Solution for an intially plane wave

To illustrate the isotropisation process, we consider an initial NIW-field that consists of a single plane wave, that is,

$$M(\boldsymbol{x}, t = 0) = M_0 e^{i\boldsymbol{k}_0 \cdot \boldsymbol{x}}, \tag{24}$$

where M_0 is a constant. Without loss of generality, we take $\boldsymbol{k}_0$ to be aligned with the x-axis, $\mathbf{k_0} = (|\mathbf{k_0}|, 0)$. From (3), the Wigner transform corresponding to (24) is

$$W_0(\boldsymbol{k}) = W(\boldsymbol{k}, t = 0) = \delta(\boldsymbol{k} - \boldsymbol{k}_0), \tag{25}$$

9

or, equivalently, in polar coordinates,

$$W_0(|\boldsymbol{k}|, \theta) = |\boldsymbol{k}_0|^{-1}\delta(|\boldsymbol{k}| - |\boldsymbol{k}_0|) \times \delta(\theta). \tag{26}$$

The Wigner transform at later times can be similarly written in separable form,

$$W(|\boldsymbol{k}|, \theta, t) = |\boldsymbol{k}_0|^{-1}\delta(|\boldsymbol{k}| - |\boldsymbol{k}_0|)W_\theta(\theta, t), \tag{27}$$

where W_θ is solution of (16) with initial condition $W_\theta(\theta, t = 0) = \delta(\theta)$. Using (21) and the Fourier series for the Dirac function

$$\delta(\theta) = \frac{1}{2\pi} + \frac{1}{\pi}\sum_{n=1}^{\infty}\cos(n\theta),$$

this can be written explicitly as

$$W_\theta(\theta, t) = \frac{1}{2\pi} + \frac{1}{\pi}\sum_{n=1}^{\infty}\mathrm{e}^{(\lambda_n - \Sigma)t}\cos(n\theta). \tag{28}$$

The influence of the background flow shows through the eigenvalues λ_n and Σ, which are both functions of $|\boldsymbol{k}|$. We compute these asymptotically and numerically for Gaussian flows in the next section.

3. Gaussian random flow

We now take the streamfunction to be an isotropic, homogeneous Gaussian process characterised by its covariance $R(\boldsymbol{x}) \propto \mathrm{e}^{-k_c^2|\boldsymbol{x}|^2/2}$. The corresponding power spectrum is

$$\hat{R}(|\boldsymbol{k}|) = A\,\mathrm{e}^{-|\boldsymbol{k}|^2/(2k_c^2)}, \tag{29}$$

for some $A > 0$, and implies a correlation length $\ell_c = 2\sqrt{2\pi}/k_c$ with the definition we have chosen [29]. For this spectrum, it is instructive to calculate approximations to the eigenvalues (19) and hence deduce the isotropisation time scale (23) in the two limiting cases $|\boldsymbol{k}| \ll k_c$ and $|\boldsymbol{k}| \gg k_c$.

First, for $|\boldsymbol{k}| \ll k_c$, $\hat{R} \sim 1$ in (14) and $\sigma'(\theta') \propto \sin^2(\theta'/2)$; in this regime, corresponding to waves of scales much larger than the flow correlation scale,

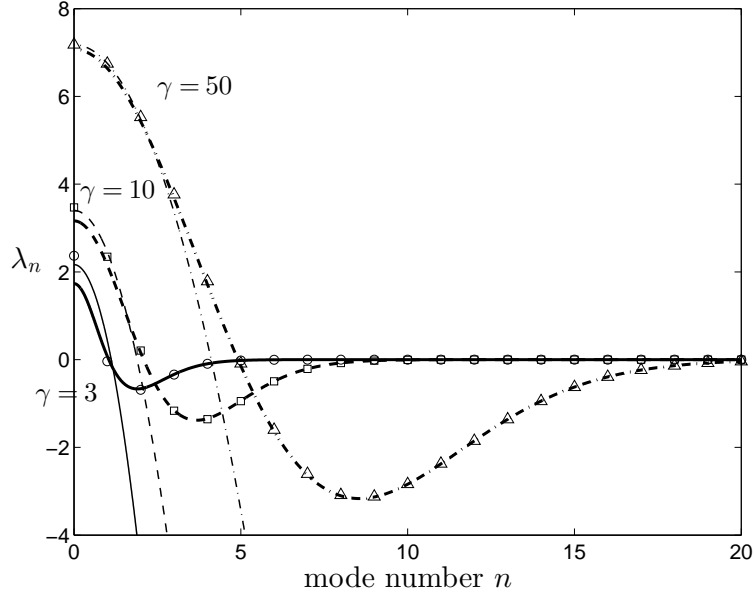$$\lambda_0 = \Sigma \sim \frac{8\pi^2|\boldsymbol{k}|^4 A}{h}, \tag{30}$$

FIG. 1. Eigenvalues of the scattering cross-section operator $\mathcal{L}$ obtained numerically (symbols) and asymptotically from (31) (thick lines) and (32) (thin lines) for $\gamma = 3$ ($\circ$ and solid line), 10 ($\square$ and dashed line) and 50 ($\triangle$ and dashed-dotted line). The eigenvalues are scaled by the factor $2\pi^{3/2} k_c^4 A/h$ appearing in (31) and (32).

while $\lambda_1 \sim -\lambda_0/2$ and $\lambda_{n \geq 2} = o(\lambda_0)$. Therefore, the isotropisation time-scale is approximately Σ^{-1}.

Second, for $|\boldsymbol{k}| \gg k_c$, using a steepest-descent method (detailed in Appendix B 1), we find

$$
\begin{aligned}
\lambda_n \sim & \frac{2\pi^{3/2} k_c^4 A}{h} \gamma^{3/2} \exp\left(\gamma(\alpha_n^{1/2} - 1)/2 - n\sinh^{-1}(2n/\gamma)\right) \\
& \times \left((\alpha_n^{-1/4} - \alpha_n^{1/4}) + \frac{1}{6\gamma}(\alpha_n^{-1/4} - \alpha_n^{-3/4} + \frac{7}{2}\alpha_n^{-5/4} + \frac{5}{2}\alpha_n^{-7/4}) \right),
\end{aligned}
\tag{31}
$$

where $\gamma = 2|\boldsymbol{k}|^2/k_c^2 \gg 1$, $\alpha_n = 1 + 4n^2/\gamma^2$, and we have assumed that $n = O(\gamma)$ to obtain an approximation uniformly valid for large n. Expression (31) is plotted in Fig. 1 as a thick line for three values of γ, along with the exact value (19) calculated numerically. The approximation (31) is accurate for $n \geq 1$, even for the moderately large $\gamma = 3$, but it fails for $n = 0$ because of the assumption $n = O(\gamma)$ breaks down. An application of Laplace's method for $n = O(1)$ detailed in Appendix B 2, gives the approximation

$$
\lambda_n \sim \frac{2\pi^{3/2} k_c^4 A}{h} \gamma^{1/2} \left(1 + \gamma^{-1}(3/4 - 3n^2)\right).
\tag{32}
$$

11

in place of (31). Expression (32) is plotted in Fig. 1 as a thin line for the three values of γ used above. The leading order of (32) agrees with (31) for $n = 0$. Moreover, from (32), λ_n decreases with n for $n = O(1)$. Combining the results (32) and (31) holding for different ranges of n, we deduce that λ_0 and λ_1 are the two largest eigenvalues of $\mathcal{L}$, with $\lambda_1 < \lambda_0$. Consequently, for $|\boldsymbol{k}| \gg k_{\mathrm{c}}$, the scattering and isotropisation time-scales are, from (32),

$$\Sigma^{-1} \sim \frac{h}{2\pi^{3/2} k_{\mathrm{c}}^4 A} \gamma^{-1/2}. \tag{33}$$

and

$$(\Sigma - \lambda_1)^{-1} \sim \frac{h}{6\pi^{3/2} k_{\mathrm{c}}^4 A} \gamma^{1/2}. \tag{34}$$

Therefore, as $\gamma \to \infty$, that is, as the wave scales decrease, the scattering time-scale decreases as $\gamma^{-1/2}$ while the isotropisation time-scale increases as $\gamma^{1/2}$. Thus NIWs with scales much smaller than the flow scales are quickly impacted by the flow but require long times to isotropise fully.

D. Importance of advection

It is interesting to examine the specific effect of advection on the scattering as this process is absent from the Schrödinger equation treated in [25]. We do this by neglecting advection and analysing how the various quantities calculated in the previous section change. Without advection, the term proportional to $|\boldsymbol{k} \times \boldsymbol{p}|^2$ disappears from (10) (see (A5)–(A8)), and (14) becomes

$$\sigma'(|\boldsymbol{k}|, \theta') = \frac{8\pi |\boldsymbol{k}|^4}{h} \sin^4(\theta'/2) \hat{R}(2|\boldsymbol{k}| \sin(\theta'/2)). \tag{35}$$

Let us now see how the change of exponent in (35) impacts on the isotropisation timescale in the two regimes studied above. In the case $|\boldsymbol{k}| \ll k_{\mathrm{c}}$, it is easy to show that

$$\Sigma = \frac{6\pi^2 |\boldsymbol{k}|^4 A}{h},$$

while $\lambda_1 = -2\lambda_0/3$, $\lambda_2 = \lambda_0/6$ and $\lambda_{n \geq 3} = o(\lambda_0)$. Therefore, the isotropisation timescale is

$$(\Sigma - \lambda_2)^{-1} = \frac{h}{5\pi^2 |\boldsymbol{k}|^4 A}. \tag{36}$$

In this case, advection only decreases the isotropisation timescale by the modest factor 5/8 (compare the inverse of (30) with (36)). Its impact is more dramatic in the case $|\boldsymbol{k}| \gg k_{\mathrm{c}}$.

12

Without advection, it is possible to show, using similar techniques as those of Appendix B, that the two largest eigenvalues are λ_0 and λ_1, so that the scattering and isotropisation timescales are

$$\Sigma^{-1} \simeq \frac{h}{3\pi^{3/2}k_c^4 A}\gamma^{1/2} \tag{37}$$

and

$$(\Sigma - \lambda_1)^{-1} = \frac{h}{15\pi^{3/2}k_c^4 A}\gamma^{3/2}. \tag{38}$$

Thus advection dramatically decreases the scattering and isotropisation timescales, by factors proportional to $1/\gamma \propto 1/|\boldsymbol{k}|^2$ (compare (33)–(34) and (37)–(38)). This is confirmed by numerical simulations (not shown).

These results can be understood physically by considering the YBJ equation (1). The regime $|\boldsymbol{k}| \ll k_c$ corresponds to $\ell_w/\ell_f \gg 1$, when advection is much smaller than refraction and has little influence the dynamics. In contrast, for $|\boldsymbol{k}| \gg k_c$ or $\ell_w/\ell_f \ll 1$, advection dominates over refraction and its effect considerably accelerates the scattering process.

E.   Numerical simulations

In this section, we validate the theoretical findings of the previous section using numerical simulations of the YBJ equation (1) for an initially plane wave. We focus particularly on the isotropisation time scale.

1.   Quantifying the isotropisation

We consider the evolution of a wavefield that is initially strongly anisotropic, with initial condition (24), corresponding to (25) or (26) in terms of Wigner transform. To analyse its scattering, we calculate the Fourier transform of M rather than its Wigner transform. This has two advantages. First, from the dimensional version of (A3),

$$W(\boldsymbol{x}, \boldsymbol{k}, t) = \int_{\mathbb{R}^2} e^{i\boldsymbol{p}\cdot\boldsymbol{x}} \hat{M}(-\boldsymbol{k} - \boldsymbol{p}/2, t)\hat{M}^*(-\boldsymbol{k} + \boldsymbol{p}/2, t)\,\mathrm{d}\boldsymbol{p}, \tag{39}$$

where $\hat{M}$ denotes the Fourier transform of M, it follows that

$$|\hat{M}(\boldsymbol{k}, t)|^2 = 4\pi^2 \int_{\mathbb{R}^2} W(\boldsymbol{x}, -\boldsymbol{k}, t)\,\mathrm{d}\boldsymbol{x}. \tag{40}$$

13

(The minus sign arises from our particular definition of the Fourier transform, see (A4).) According to the perturbation theory of Appendix A, the leading-order Wigner transform is spatially independent and the higher-order terms have vanishing spatial averages when there is no large-scale dependence on the initial condition and velocity field, as assumed here (see (A9)). Therefore, $|\hat{M}(\boldsymbol{k}, t)|^2$ directly measures the leading-order Wigner transform. Second, the analysis is obviously much easier with the reduction from the five dimensions of the Wigner transform to the three dimensions of the Fourier transform.

A natural measure of the isotropy of the wave field is the ratio r of the kinetic energy associated with the right-hand part of the Fourier spectrum ($k > 0$) to the total kinetic energy,

$$r(t) = \frac{1}{E} \iint_{k>0, l} |\hat{M}(\boldsymbol{k}, t)|^2 \, \mathrm{d}\boldsymbol{k}, \tag{41}$$

where E is the integral appearing in (41) extended over the entire (k, l)-plane. An isotropic field is thus characterized by $r = 0.5$ and the initial condition (24) by $r(0) = 0$. We choose this measure over more sophisticated ones because (i) it is easy to calculate without the need to resort to polar coordinates, (ii) the large domain of integration (a half plane in (k, l)) gives a measure that is smooth in time.

As described in section III C 2, the initial condition (25) leads to an exact solution given by (28)–(27) for the Wigner transform. Using this and (40), we compute the ratio r for this solution as

$$\begin{aligned} r(t) &= \frac{4\pi^2 S}{E} \int_{\pi/2}^{3\pi/2} W_\theta(\theta, t) \, \mathrm{d}\theta \\ &= \frac{1}{2} - \frac{2}{\pi} \sum_{n=0}^{\infty} \frac{(-1)^n}{2n+1} \mathrm{e}^{-(\Sigma - \lambda_{2n+1})t}, \end{aligned} \tag{42}$$

where S is the area of the domain. The second term in (42) tends to 0 as $t \to \infty$.

2. Parameters and results

Equation (1) is solved on a doubly periodic 512×512 grid using a pseudo-spectral time-split Euler scheme. A weak biharmonic dissipation is added for numerical stability. The streamfunction ψ is taken as a realization of a homogeneous isotropic Gaussian random field, with power spectrum (29) with the correlation length $\ell_c = 200$ km. It is time-independent but, according to Appendix A, any time dependence with stationary statistics would lead
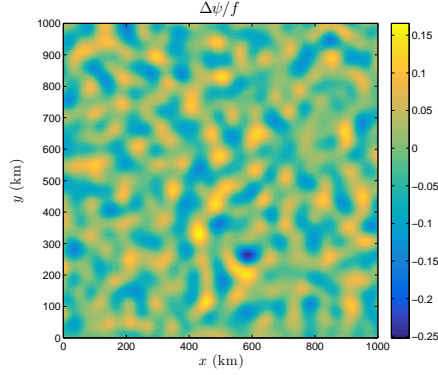
14

FIG. 2. Vorticity field, normalised by the Coriolis frequency f, for one realisation of the Gaussian random streamfunction with power spectrum (29) and correlation length 200 km.

to the same results provided that it is slow compared with the wave time scale. The domain is a square of length $40\ell_c = 8000$ km. The Coriolis frequency is $f_0 = 10^{-4}\text{s}^{-1}$ and the Rossby radius of deformation is $r_d = 20$ km, representative of the North Atlantic; this gives a dispersion parameter $h = f_0 r_d^2 = 4 \cdot 10^4 \, \text{m}^2 \, \text{s}^{-1}$. We verify that, because $(f_0^2 + f_0 h (2\pi/\ell_c)^2)^{1/2} - f_0 \simeq 2 \cdot 10^{-5} \ll f_0$, waves with a similar wavelength as the background flow satisfy the near-inertial approximation. The amplitude A of the power spectrum is chosen such that the root-mean-square of the vorticity field is $\zeta_\text{rms} \simeq 5 \cdot 10^{-6}\text{s}^{-1} \ll f_0$. Thus, the parameter $\Psi/h = (\ell_c/(2\pi))^2 \zeta_\text{rms}/h \simeq 0.12$ is much smaller than 1, in accordance with the scaling used in Appendix A. A typical subdomain of size $1000\,\text{km} \times 1000\,\text{km}$ of the vorticity field is shown in Fig. 2.

Three different values of the parameter $\gamma = 2|\boldsymbol{k}_0|^2/k_c^2$ are used: $\gamma = 0.5$, 1.1 and 4.9, corresponding to a NIW wavelength $2\pi/|\boldsymbol{k}_0|$ of approximately 500, 340 and 160 km. Fig. 3 displays the evolution of M, specifically Re M alongside the magnitude of its Fourier transform $|\hat{M}|$, for $\gamma = 1.1$. As expected, the initially unidirectional wave field (Fig. 3a) is slowly modulated by the flow, leading to the generation of fluctuations in all directions (Figs. 3c, e), and ends up almost isotropic (Fig. 3g). This is confirmed by the amplitude of the Fourier transform $|\hat{M}|$ (Fig. 3, right column), which starts from a single point $(-|\boldsymbol{k}_0|, 0)$ in the (k, l)-plane (Fig. 3b), then develops into a thin annulus of radius $|\boldsymbol{k}_0|$ as the energy at $(-|\boldsymbol{k}_0|, 0)$ decreases (Figs. 3d, f, h).

For each value of γ, simulations like the one used for Fig. 3 have been repeated 20 times with different realisations of the streamfunction. From these simulations, we calculate the
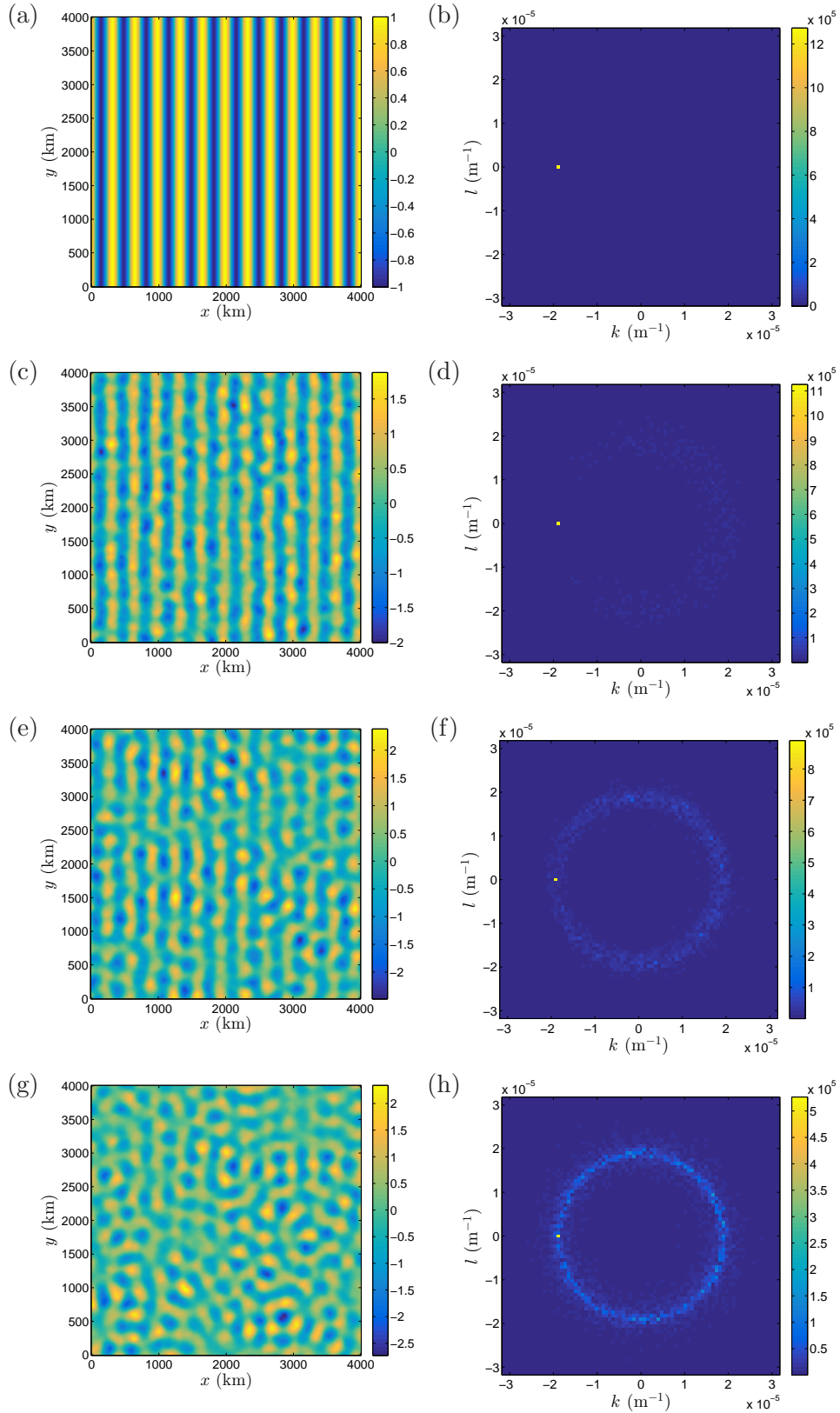
15

FIG. 3. Evolution of Re M in a 4000 km×4000 km subdomain (left), and of the Fourier transform amplitude $|\hat{M}|$ for an initially plane wave, shown at $t = 0$ (a, b), 10 days (c, d), 30 days (e, f) and 75 days (g, h) for $\gamma = 1.1$ (see text for the value of other parameters).
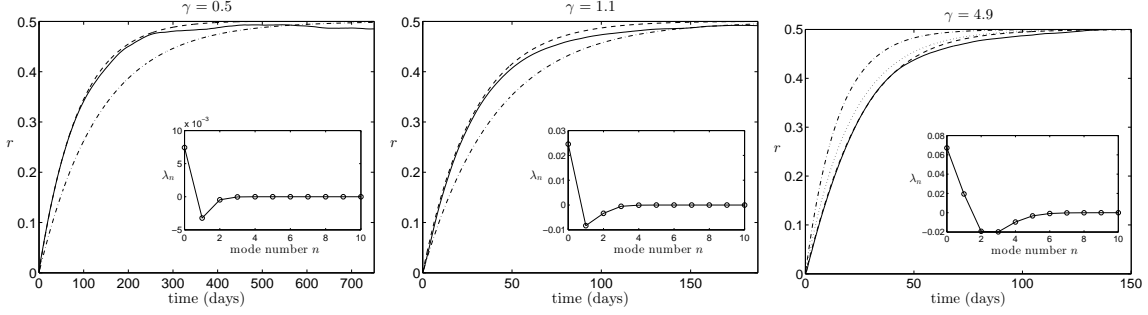
FIG. 4. Evolution of the energy ratio r defined in (41) for $\gamma = 2k_0^2/k_c^2 = 0.5$ (left), 1.1 (middle) and 4.9 (right). The average ratio calculated from 20 simulations for each value of γ (solid lines) is compared with the theoretical prediction (42) (dashed lines) and with the approximations $r_\Sigma = (1 - \exp(-\Sigma t))/2$ (dash-dotted lines) and $r_{\lambda'} = (1 - \exp(-(\Sigma - \lambda')t))/2$ (dotted lines). For $\gamma = 0.5$ and 1.1, $r_{\lambda'}$ is indistinguishable from r_Σ. Note the different time ranges in each figure. The eigenvalues λ_n defined in (19) are shown in the insets. Units of r and λ_n are days^{-1}.

average of the ratio $r(t)$ defined in (41). Fig. 4 displays the evolution of this ratio for the three values of γ, together with the theoretical prediction (42) and the two estimates

$$r_\Sigma(t) = \frac{1}{2}\left(1 - e^{-\Sigma t}\right) \text{ and } r_{\lambda'}(t) = \frac{1}{2}\left(1 - e^{-(\Sigma - \lambda')t}\right), \tag{43}$$

where λ' is defined in (23). These are crude estimates based on the scattering and isotropisation time scales Σ^{-1} and $(\Sigma - \lambda')^{-1}$. The agreement between the numerical simulations (solid line) and the theoretical prediction (dashed line) is excellent, considering the strong assumptions underlying the derivation of (16). The estimates r_Σ and $r_{\lambda'}$ offer good, albeit less accurate, approximations. In particular, for $\gamma = 4.9$, $r_{\lambda'}$ offers a significant improvement over r_Σ, highlighting the fact that $(\Sigma - \lambda')^{-1}$ is a more appropriate time-scale for isotropisation than Σ^{-1}.

From Fig. 4, the isotropisation e-folding time-scale is approximately 81, 27 and 23 days for $\gamma = 0.5$, 1.1 and 4.9. This is in agreement with expression (30) for small γ: as γ or $|\boldsymbol{k}|$ decreases, the time-scale increases. For γ larger than 4.9, we expect the isotropisation time-scale to increase again, in agreement with (34). The relatively short isotropisation time scale found for $\gamma = 1.1$ and 4.9 is comparable with other time scales relevant to NIW dynamics, such as the vertical propagation time scale (see Ref. 19) – a phenomenon absent here because of the simplified reduced-gravity shallow-water setup – or the β-dispersion time

17

scale $|\boldsymbol{k}|/\beta$.

IV. APPLICATIONS

We now consider two physical scenarios in which scattering plays an important role. Scattering has the most dramatic impact on waves that would be unidirectional in the absence of flow, as it then leads to dispersion in multiple directions instead. Examples of such waves in the ocean are inertial waves propagating equatorward due to the β-effect, and inertial waves generated by a moving cyclone. We examine these two types of waves in what follows, using simulations of a reduced gravity shallow-water model of the mixed-layer (cf. Ref. 20, section 4). This model reduces to the YBJ model of the previous sections when the near-inertial and linear approximations are made. By relaxing these approximations, we confirm the relevance of the theoretical results to the more realistic setup. We continue to assume a time-independent flow, an assumption that should not alter the results provided the flow evolves slowly enough.

A. Wavepacket on a β-plane

For large spatial and time scales, the β-effect associated with the earth's curvature becomes important. As a result, waves develop a zonally banded structure characterized by negative meridional wavenumbers and equatorward propagation, as described by a ray-tracing (WKB) approximation. Such waves are ubiquitous in global simulations [30, 31] and oceanic measurements [32]. Although this process is well understood in simple configurations [33], the additional effect of a background flow remains, to our knowledge, unexplored. As we shall see, this effect can, under some circumstances, strongly affect the wave properties.

We examine the propagation of a NIW packet in a region of strong geostrophic turbulence. Taking the β-plane approximation $f = f_0 + \beta y$ with $f_0 = 1.16 \cdot 10^{-4}\mathrm{s}^{-1}$ and $\beta = 1.37 \cdot 10^{-11}\,\mathrm{m}^{-1}\mathrm{s}^{-1}$ (corresponding to a latitude of 53°N), we carry out simulations of an unforced problem, with initial conditions

$$(u, v, \eta)(x, y, t = 0) = (\cos(l_0 y), \omega \sin(l_0 y)/f_0, H l_0 \sin(l_0 y)/f_0) u_0 \, \mathrm{e}^{-|\boldsymbol{x}|^2/(2L^2)},$$

that represent a Gaussian wavepacket satisfying the polarisation relations of inertia-gravity waves. Here, (u, v) is the velocity field, η is the perturbation of the mixed-layer depth from

18

its average value $H = 50$ m, $l_0 = -2\pi/(180\,\text{km})$ is the initial meridional wavenumber, and $\omega = \sqrt{f_0^2 + g'Hl_0^2} \simeq 1.21 \cdot 10^{-4}\,\text{s}^{-1}$, with $g' = 0.02\,\text{m s}^{-2}$, obeys the inertia-gravity-wave dispersion relation. The other parameters are $L = 710$ km and $u_0 = 0.2\,\text{cm s}^{-1}$, a value small enough to ensure that the wave–wave interaction terms remain small; it could be increased without affecting much the overall dynamics. Fig. 5a displays the initial zonal wave velocity $u(x, y, t = 0)$.

We compare the wave dynamics in a reference simulation without flow and in an ensemble of 20 simulations with flows taken as realisations of a (time-independent) homogeneous and isotropic Gaussian random process with Gaussian correlation function. The r.m.s. of the vorticity field in these flows is $\zeta_{\text{rms}} = 2.6 \cdot 10^{-6}\text{s}^{-1}$, and the streamfunction correlation length is 310 km. A 1000×1000 km close-up of the vorticity field in one flow realisation is displayed in Fig. 5b.

Fig. 5c illustrates the wavepacket behaviour in the absence of flow by showing the kinetic energy density after 30 days. As expected, the wavepacket drifts equatorward, by a distance $\Delta y \simeq -1100$ km that can be estimated using ray tracing, while the wavenumber decreases to $-6.7 \cdot 10^{-5}\text{m}^{-1}$ to satisfy the dispersion relation. The picture changes considerably in the presence of a flow. Fig. 5d shows the kinetic energy density averaged over the 20 flow realisations; clearly, the wavepacket drifts more slowly equatorward while spreading out more. Fig. 6 shows the zonal (panel a) and meridional (panel b) integrals of the kinetic energy density in Fig. 5. The location of the wavepacket calculated from ray tracing is indicated by a vertical line in panel b and matches closely the numerical simulation without flow. The slowdown of the meridional drift and the increase spread in the presence of the flow are evident. To quantify them we define the drift $\bar{\boldsymbol{x}}$ and spread σ of the wave kinetic energy distribution $E(\boldsymbol{x})$ from its first and second moments,

$$\bar{\boldsymbol{x}} = \frac{\int \boldsymbol{x}E(\boldsymbol{x})\,\mathrm{d}\boldsymbol{x}}{\int E(\boldsymbol{x})\,\mathrm{d}\boldsymbol{x}} \quad \text{and} \quad \sigma^2 = \frac{\int |\boldsymbol{x} - \bar{\boldsymbol{x}}|^2 E(\boldsymbol{x})\,\mathrm{d}\boldsymbol{x}}{\int E(\boldsymbol{x})\,\mathrm{d}\boldsymbol{x}}.$$

After 30 days, the average meridional drift in the simulations with flow is $\bar{y} \simeq -650$km, much smaller than without flow. The spread with flow is about $\sigma = 950$ km, larger than its initial value 710 km and the final value without flow, about 750 km. Results are more dramatic for longer times, but our neglect of vertical propagation then becomes problematic.

The results detailed above are consistent with the scattering process described earlier in the paper. Let us first note that the β-effect can be added to the YBJ equation (1) and
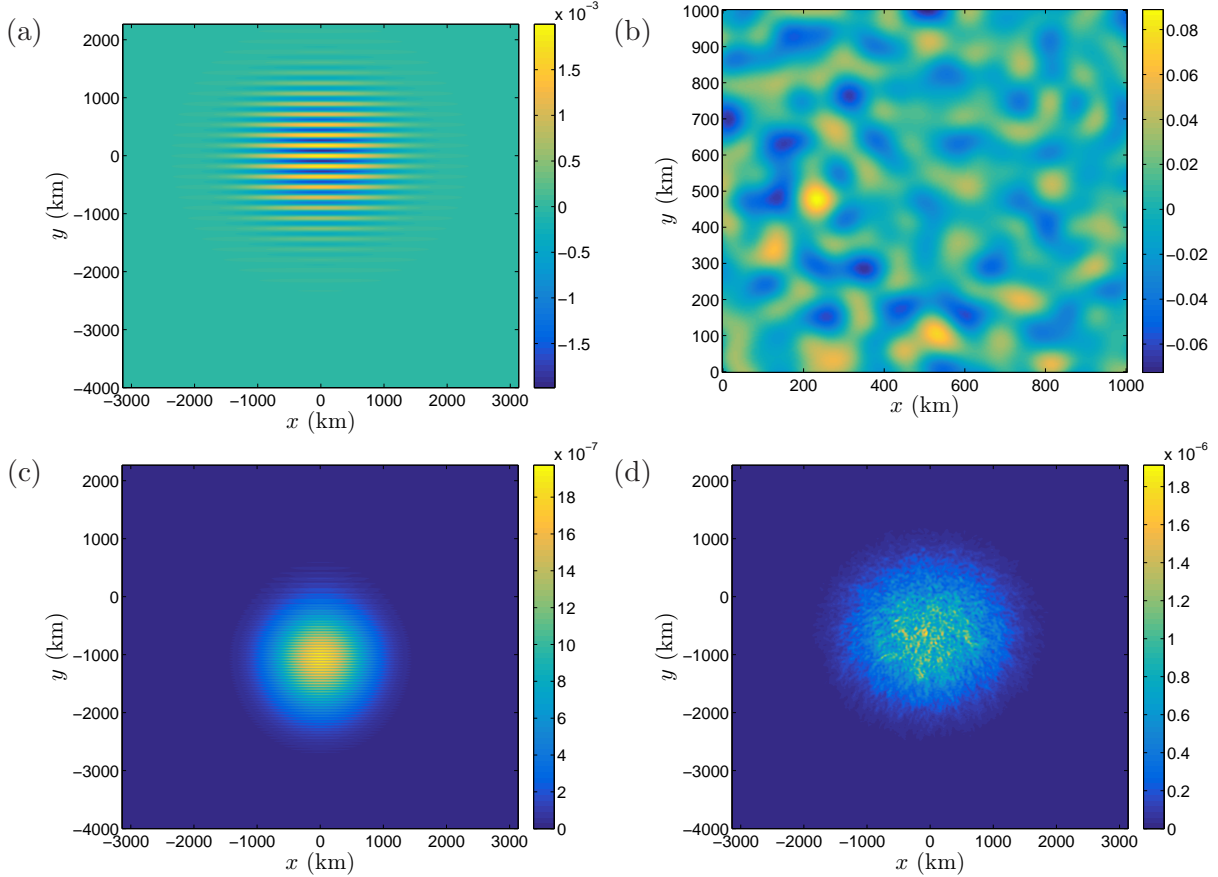
FIG. 5. Wavepacket on a β-plane: (a) zonal velocity at the start of the simulations; (b) example of the relative vorticity field (scaled by the Coriolis frequency f_0) used in one of the twenty runs, shown in a subdomain of size 1000×1000 km; (c) inertial kinetic energy after 30 days for the simulation with no background flow; (d) inertial kinetic energy after 30 days averaged over 20 flow realisations.

leads to the extra term $i\beta y M$ on the left-hand side. This modifies the transport equation (7) by adding a transport in spectral space with velocity $-\beta$ in the l-direction,

$$\partial_t W + h\boldsymbol{k} \cdot \boldsymbol{\nabla}_{\boldsymbol{x}} W - \beta \partial_l W = \mathcal{L}W - \Sigma(\boldsymbol{k})W, \tag{44}$$

where $\boldsymbol{k} = (k, l)$. For brevity, we do not provide a derivation but refer the reader to the general form of the transport equation for a dispersion relation that depends on both $\boldsymbol{k}$ and $\boldsymbol{x}$ (Ref. 25, Eq. (1.1)). In the absence of a flow, the transport in spectral space is equivalent to the evolution of the meridional wavenumber $l(t) = l_0 - \beta t$ in the WKB approximation.

Qualitatively, (44) implies an interplay between β-effect and scattering by the flow, the former transferring energy to smaller meridional wavenumbers (larger in magnitude since
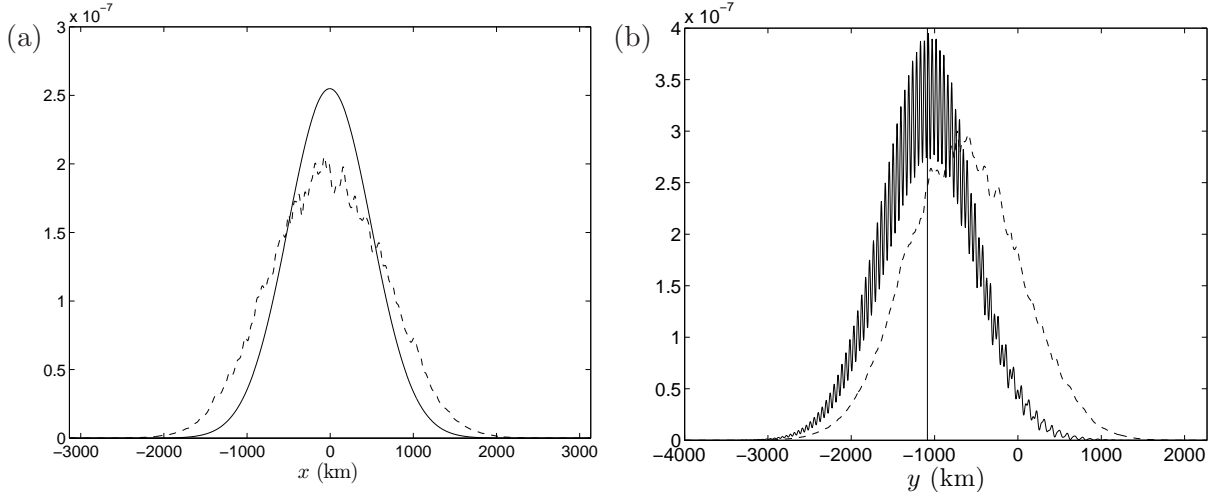
20

FIG. 6. Horizontal kinetic energy of the wavepacket on a β-plane: (a) meridional average in the simulation with no flow (solid line, see Fig. 5c) and in the 20 simulations with flow (dashed line, see Fig. 5d), (b) same as (a) but with a zonal average instead. The black vertical line in (b) indicates the location of the wavepacket as predicted by WKB theory.

they are negative), the latter redistributing energy between wavevectors of the same magnitude. This interpretation is confirmed by simulations. Fig. 7 shows the zonal velocity after 30 days without flow (panel a) and in one of the flow realisations (panel c), along with the amplitude of the Fourier transform of $u + iv$ (equivalent to $|\hat{M}|$ for NIWs), without flow (panel b), and averaged over the 20 simulations in the case with flow (panel d). Fig. 7d shows that, as energy is transferred to smaller meridional wavenumbers due to the β-effect, it is also transferred to other wavenumbers in a quasi-isotropic way. Because these two processes are concurrent, the energy distribution in spectral space is much more complex than the annulus obtained without β (Fig. 3h). Its shape is close to a circular arc with an energy maximum at $l(t) = l_0 - \beta t$ and with a radius of curvature smaller than $|l(t)|$, reflecting the scattering history. Note that the reason why neighbouring wavevectors are excited first, in contrast with the simulation of Fig. 3 is the larger value of $|l(t)|/k_c$, where k_c is related to the flow correlation length through $k_c = 2\sqrt{2\pi}/\ell_c$. Here, $\gamma = 2(l(t)/k_c)^2$ is close to 34 after 30 days (i.e. waves have much smaller scales than the flow), a value much larger than the value 1.1 used for Fig. 3.

As expected from the spectrum in Fig. 7d, the zonal velocity field (Fig. 7c) displays a variety of wavelengths, with short waves at the front of the wavepacket and longer waves at
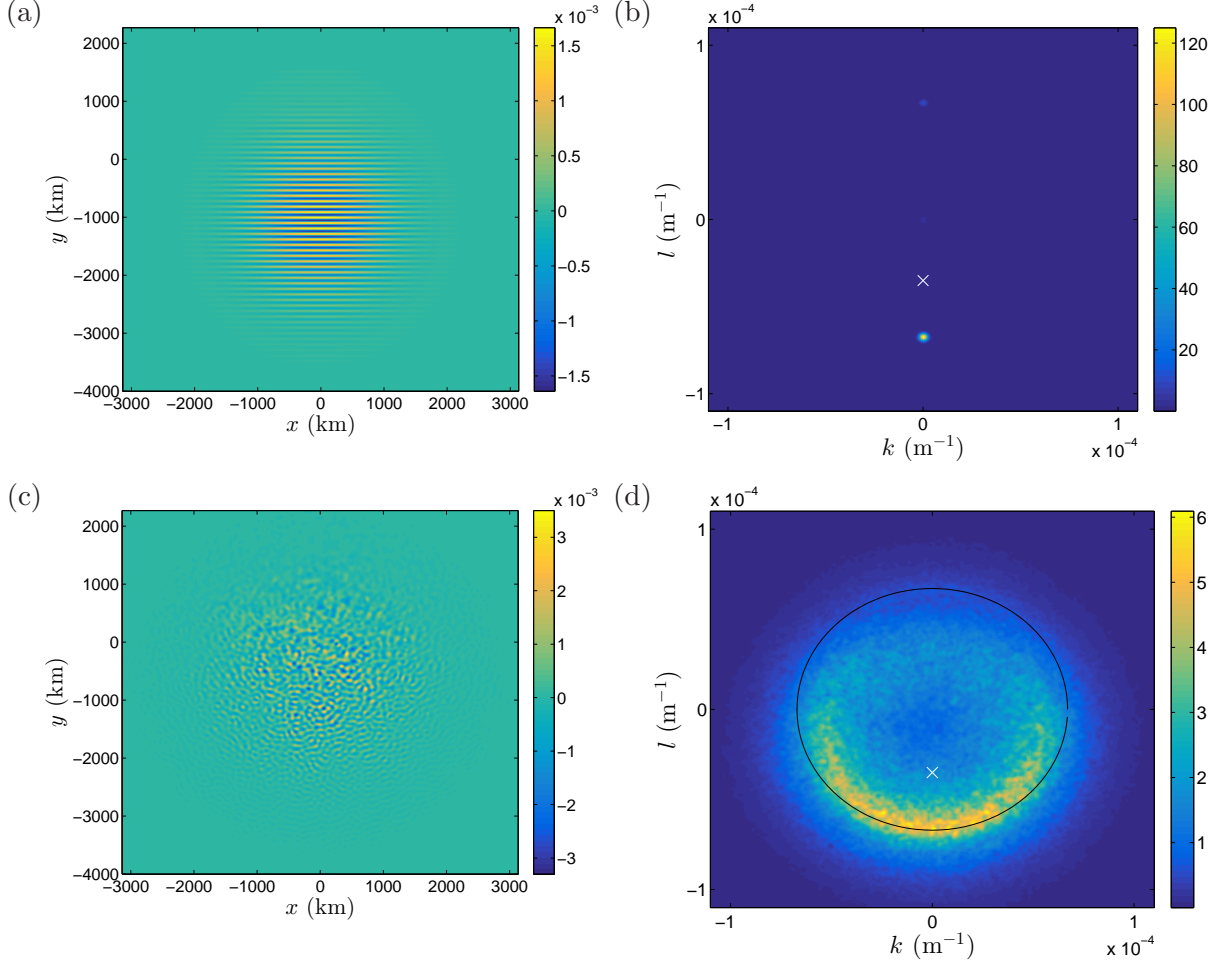
21

FIG. 7. Wavepacket on a β-plane: zonal velocity (panels a, c) and amplitude of the Fourier transform $|\hat{u} + i\hat{v}|$ (panels b,d) after 30 days in the simulations without (a, b) and with flow (c, d). Panel c shows the zonal velocity in one particular flow realisation whereas panel d shows an average over 20 simulations. Initially the Fourier transform is concentrated in a narrow region centered on $(k, l) = (0, -3.5 \cdot 10^{-5})$ represented here by a white cross. The circle in panel d has a radius equal to $|l(30\text{days})| = 6.7 \cdot 10^{-5} \text{m}^{-1}$ (see text).

the back, while the local wavevector is deflected from its initial North-South orientation into a broad range of directions, causing the spreading of the wavepacket. We can verify that the time scales associated with the β-effect and with scattering are comparable: the former is $l_0/\beta = 29$ days; the latter can be estimated by taking the wavenumber as $l(t) = l_0 - \beta t$ to find $\Sigma^{-1} = 5$ days and $(\Sigma - \lambda')^{-1} = 15$ days for $t = 0$, and $\Sigma^{-1} = 3$ days and $(\Sigma - \lambda')^{-1} = 32$ days for $t = 30$ days.

B. Moving cyclone

A moving cyclone generates a wake of internal waves which is stationary in the cyclone reference frame, much like the surface-wave wake generated by a moving ship. Due to resonance, the most energetic waves to emerge are NIWs with a wavenumber $k \sim f_0/U$ in the direction of translation of the cyclone. Here, f_0 and U are the Coriolis frequency and cyclone translation speed. A typical value for U is 5 m s^{-1}, giving a wavelength $2\pi U/f_0 \sim 300 \text{ km}$ at mid-latitudes, close to the most energetic scales in the ocean [34]. Moving cyclones have been studied in detail both in the linear [35–37] and nonlinear contexts [38–43]. Importantly, all these studies neglect the influence of a background flow by considering an ocean initially at rest. Therefore, there is a clear need to analyse the propagation of cyclone-generated NIWs in the presence of a turbulent flow.

Motivated by this, we examine shallow-water simulations of a moving cyclone in 20 real-isations of the random flow used in the previous section ($\zeta_{\text{rms}} = 2.6 \cdot 10^{-6} \text{ s}^{-1}$, $\ell_{\text{c}} = 310 \text{ km}$) and, for comparison, one simulation without any flow. In our simulations, the cyclone is represented by a wind stress of the form $\boldsymbol{\tau} = \tau_\theta(r)\boldsymbol{e}_\theta$ in a polar coordinates system translating steadily in the eastward direction. The radial profile of the wind stress is

$$\tau_\theta(r) = \begin{cases} \tau_{\text{max}}r/R & \text{for } r < R \\ \tau_{\text{max}}(1.2 - 0.2r/R) & \text{for } R \leq r \leq 6R \\ 0 & \text{for } r > 6R \end{cases}$$

(see Ref. 44). The cyclone translation speed is $U = 2 \text{ ms}^{-1}$ and the radius of maximum stress is $R = 75$ km, making this a relatively wide and slow-moving cyclone. The stress field described above is applied homogeneously throughout the top layer as a body force $\boldsymbol{\tau}/(\rho_0 H)$, where $H = 100$ m is the average mixed layer depth and $\rho_0 = 1025 \text{ kg m}^{-3}$ is a reference density. To avoid spurious wave emission, τ_{max} is progressively increased from zero to the value $\tau_{\text{max}} = 0.75 \text{ N m}^{-2}$ (corresponding roughly to 90 km/h winds) during the first two days, and damped after 16 days, before the cyclone, which originates from the western boundary of the domain, hits the eastern boundary. The Coriolis frequency is taken as $f_0 = 7 \cdot 10^{-5} \text{ s}^{-1}$, corresponding to a latitude of 30°N; the β effect is neglected for simplicity. Finally, we take $g' = 0.01 \text{ m s}^{-2}$, giving the same short-wave speed $c = (g'H)^{1/2} = 1 \text{ m s}^{-1}$ as in the previous section.

Fig. 8 shows the NIW velocity – extracted from the total velocity field using a time
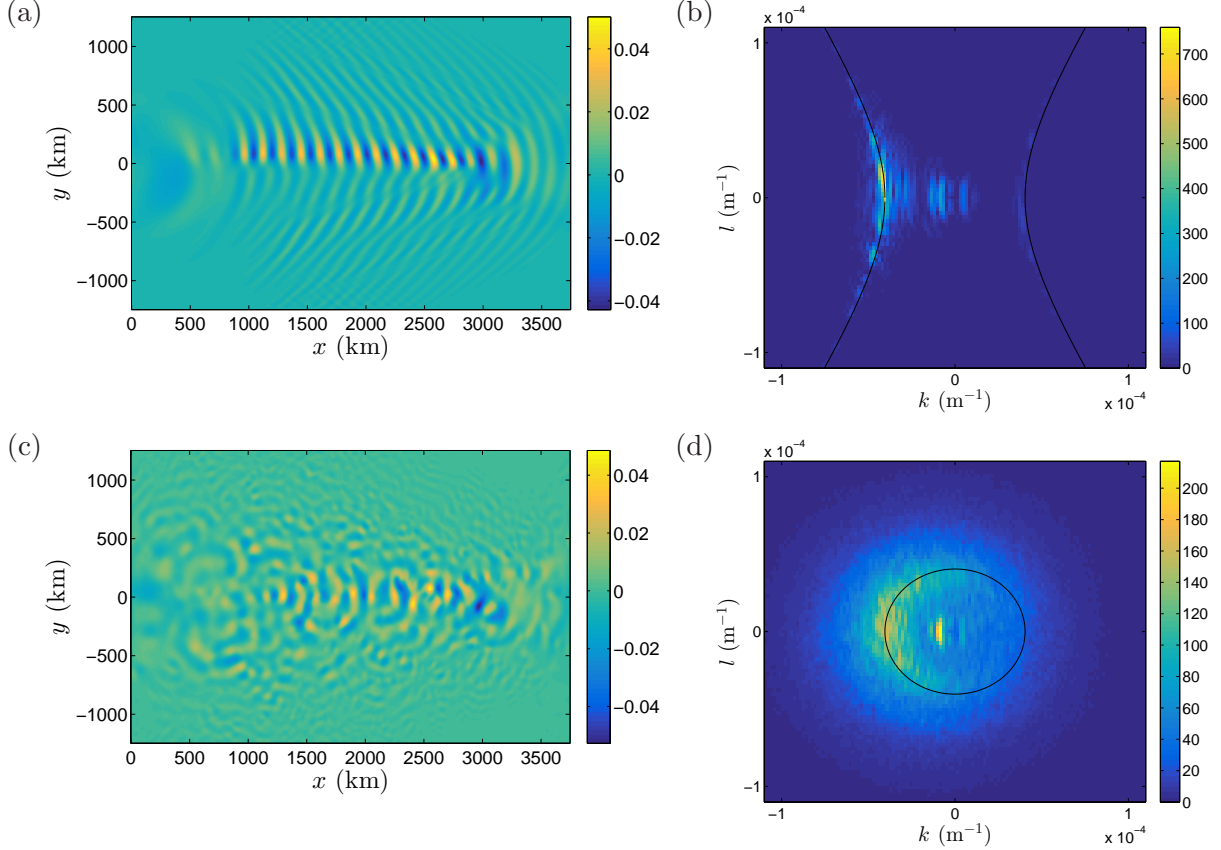
FIG. 8. NIWs generated by a moving cyclone: near-inertial zonal velocity (panels a, c) and amplitude of the Fourier transform $|\hat{u} + i\hat{v}|$ (panels b, d) after 25 days in the simulations without (panels a, b) and with flow (panels c,d). Panel c shows the field in one flow realisation, whereas panel d shows an average over 20 flow realisations. The dispersion relation $(U^2 - c^2)k^2 = f_0^2 + c^2 l^2$ and isotropic circle $k^2 + l^2 = f_0^2/(U^2 - c^2)$ are indicated by solid lines in panels b and d, respectively.

filter – with and without flow, in physical and spectral spaces, after 25 days. Without flow, the wave field generated by a moving cyclone is approximately stationary in the cyclone frame (panel a). The weak North-South asymmetry arises from nonlinear effects, which become significant for wind stresses larger than $\tau_{\max} = 0.75 \, \mathrm{N \, m^{-2}}$. As time progresses, NIWs spread laterally and the energy at $y = 0$ is significantly reduced. Fig. 8b show that the waves follow the dispersion relation for stationary waves in the cyclone reference frame, $(Uk)^2 = f_0^2 + c^2(k^2 + l^2)$ (solid lines, see Ref. 36); the energy is concentrated on one branch of the dispersion relation, which can be explained by the anticyclonic rotation rate of NIWs. Note that the energy is not distributed evenly along the dispersion curve: it is maximum
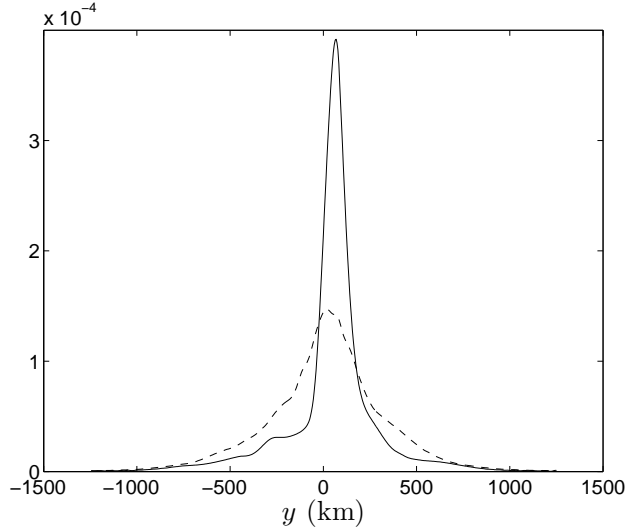
24

FIG. 9. NIWs generated by a moving cyclone: zonal average of the NIW horizontal kinetic energy in the simulation with no flow (plain line, see Fig. 8c) and the 20 simulations with flow (dashed line) after 25 days.

at $(k, l) \sim (k_G, 0)$, where $k_G = f_0/(U^2 - c^2)^{1/2}$ is the Geisler wavenumber [35] (for $c \ll U$, $k_G \sim f_0/U$). Some energy is also present at smaller wavenumbers, possibly due to filtering errors.

The NIWs are significantly affected by the presence of a flow. In particular, they display small-scale variability in the y-direction (Fig. 8c), with a velocity field that is reminiscent of Figs. 3g and 7c. The magnitude of the Fourier transform $|\hat{u} + i\hat{v}|$ averaged over the simulations with flow is illuminating (Fig. 8d): the energy appears to have spread partially along a circle of radius k_G, although a maximum is still present at $(k_G, 0)$. The relatively broad structure of energy along the isotropic circle ($k^2 + l^2 = k_G^2$) stems from nonlinear interactions (not taken into account in the theory): experiences with smaller $\tau_{\max}$ have a more concentrated NIW energy distribution (not shown).

The results described above can be interpreted in the light of the scattering theory. The scattering and isotropisation time-scales calculated from the flow characteristics and the Geisler wavenumber are respectively 4 and 23 days, of the order of the simulations length. A notable consequence of the (partial) isotropisation process is the acceleration of the lateral dispersion of NIW energy, as illustrated in Fig. 9: the flow deflects waves from their mainly zonal path (Figs. 8a,b), so that they propagate with a finite angle $\theta = \tan^{-1}(l/k)$ with the

25

x-axis (Figs. 8c,d). As a consequence, energy is transported faster away from the centre of the domain $y = 0$.

V. DISCUSSION

In this paper, we examine the impact of a complex, turbulent flow on the propagation of wind-driven near-inertial oceanic waves. We focus on the distinguished regime in which the spatial scale of the flow is comparable to the typical wavelengths. NIWs in this regime are well described by the asymptotic model due to Young and Ben Jelloul [19] on which our analysis relies. Further simplifications arise from two assumptions made on the flow: first, that its effect is weak compared to dispersion, and second that it can be modelled by a homogeneous stationary random process. With these assumptions, a transport equation governing the energy transfers in physical and spectral spaces is derived, following the general treatment of Ryzhik *et al.* [25]. This equation describes, in particular, the scattering effect of the flow, which redistributes energy along constant-wavenumber circles in spectral space. For isotropic flows, this ultimately leads to an isotropic wave field, with a scale that is essentially the same as the initial scale. Thus, in the regime considered, dispersion strongly inhibits the cascade to small scales that refraction and advection by the flow can induce. Two time scales are relevant to the scattering process: the first estimates the time necessary for scattering to be significant, the second the time to achieve isotropisation. Explicit expressions are available for both, with asymptotic expressions showing that they can be very different.

The theoretical results based on the transport equation derived from the YBJ model are shown to be relevant to the full shallow-water model in two applications. The first is motivated by the observed equatorward propagation of NIWs due to the β-effect, the second by the generation of mesoscale NIWs in the wake of moving cyclones. In both cases, the isotropisation caused by scattering strongly affects the wave field.

While our work is focussed on NIWs, it can be placed in the more general context of wave–potential-vorticity (PV) interaction. In particular, it is related to work by Lelong and Riley [45], Bartello [46] and Ward and Dewar [47] who consider the triadic interactions between the normal modes of the linear equations, namely internal (or inertia-gravity) waves and the PV (or vortical) mode. One of the four triadic interactions identified involves a wave-wave-PV resonant triad in which the PV mode, although unaffected, acts as a catalyst for

energy transfers between two indentical-frequency waves. This is precisely the interaction that our transport equation captures. We note that this transport equation is derived under the assumption of a given flow, that is, a (possibly time-dependent) PV mode determined a priori; the weakly nonlinear approach of [45–47] makes no such assumption but nonetheless leads to nearly constant PV modes as a result of PV conservation.

The most important feature of the interactions between wave modes catalysed by the flow is that it leads to energy exchanges between waves with the same frequency – circles in Fourier space for the shallow-water model of the present paper and of [47], cones for the continuously stratified models of [45, 46]. Our assumption of a flow well modelled by a homogeneous random process makes it possible to quantify these exchanges (see Müller and Xu [48] for the derivation of a transport equation relevant in the presence of a random topography). One possible extension beyond the near-inertial regime could be to internal tides, following from the recent simulations of Ponte and Klein [49] which show the emergence of spatially complex tidal signal in the presence of a turbulent flow.

We finally note that our conclusion of a relaxation to an isotropic stationary wave-energy distribution – corresponding to a uniform energy along constant-frequency curves (circles) in Fourier space – applies to the shallow-water model but not to the continuously stratified models: for these, the constant-frequency surfaces (cones) are non-compact, and it is therefore impossible for a finite wave energy to relax to a uniform distribution. It would be desirable to obtain the transport equation corresponding to these models and study the associated scattering. We leave this for future work.

Appendix A: Derivation of the transport equation

In this Appendix, we derive a transport equation for the Wigner function associated with NIWs following [25]. This is achieved by assuming a separation between the (small) scale of variation of the phase of the NIWs and the (large) scale of variation of their envelope. The ratio of these two scales is the small parameter $\epsilon \ll 1$. Another key assumption is that the background flow varies on the same scale as the NIW phase.

1. Scaled YBJ equation and Wigner function

Because we assume that the NIW amplitude varies on the large scale L, it is clear from (4) that the leading-order Wigner function depends on the large scale only. Therefore, it is natural to work with the dimensionless spatial variable $\boldsymbol{x}' = \boldsymbol{x}/L$. We emphasise that this is just a convenient change of coordinate which does not imply that M varies on the large scale; indeed with this choice, $|\boldsymbol{\nabla}_{\boldsymbol{x}'}M| = O(\epsilon^{-1})$. We assume the scaling $\Psi/h = O(\epsilon^{1/2})$ for the streamfunction of the background flow and, correspondingly, introduce the dimensionless streamfunction $\psi' = \epsilon^{-1/2}\psi/h$. This varies over the short spatial scale ℓ and thus should be regarded as a function of $\boldsymbol{\xi} = \epsilon^{-1}\boldsymbol{x}' = \boldsymbol{x}/\ell$: $\psi = \psi(\boldsymbol{\xi}, t)$. Introducing the non-dimensional time $t' = ht/(\epsilon L^2)$, we rewrite (1) in non-dimensional form

$$\partial_t M + \epsilon^{1/2}\boldsymbol{\nabla}_{\boldsymbol{\xi}}^{\perp}\psi \cdot \boldsymbol{\nabla}_{\boldsymbol{x}}M - \epsilon\frac{\mathrm{i}}{2}\Delta_{\boldsymbol{x}}M + \mathrm{i}\epsilon^{-1/2}\frac{\Delta_{\boldsymbol{\xi}}\psi}{2}M = 0, \tag{A1}$$

where primes have been omitted and the streamfunction is assumed to vary over the same slow time scale $\epsilon L^2/h = L\ell/h$ as the Wigner function. The correct scaling for the Wigner function in the scale-separation regime is

$$W^{\epsilon}(\boldsymbol{x}, \boldsymbol{k}, t) = \epsilon^{-2}W(\boldsymbol{x}, \boldsymbol{k}/\epsilon, t) = \frac{1}{4\pi^2}\int \mathrm{e}^{\mathrm{i}\boldsymbol{k}\cdot\boldsymbol{y}}M(\boldsymbol{x} - \epsilon\boldsymbol{y}/2, t)M^*(\boldsymbol{x} + \epsilon\boldsymbol{y}/2, t)\,\mathrm{d}\boldsymbol{y}. \tag{A2}$$

Note the interesting dual property

$$W^{\epsilon}(\boldsymbol{x}, \boldsymbol{k}, t) = \epsilon^{-2}\int \mathrm{e}^{\mathrm{i}\boldsymbol{p}\cdot\boldsymbol{x}}\tilde{M}(-\epsilon^{-1}\boldsymbol{k} - \boldsymbol{p}/2, t)\tilde{M}^*(-\epsilon^{-1}\boldsymbol{k} + \boldsymbol{p}/2, t)\,\mathrm{d}\boldsymbol{p}, \tag{A3}$$

where

$$\tilde{M}(\boldsymbol{p}, t) = \frac{1}{4\pi^2}\int \mathrm{e}^{\mathrm{i}\boldsymbol{p}\cdot\boldsymbol{x}}M(\boldsymbol{x}, t)\,\mathrm{d}\boldsymbol{x} \tag{A4}$$

is the Fourier transform of M with respect to $\boldsymbol{x}$ at wavevector $\boldsymbol{p}$.

2. Evolution equation for the Wigner function

Differentiating (A2) with respect to t and using (A1) yields, after some manipulations involving (A3),

$$
\begin{aligned}
\partial_t W^\epsilon &+ \frac{\epsilon^{1/2}}{2} \nabla_{\boldsymbol{x}} \cdot \int \hat{\boldsymbol{v}}(\boldsymbol{l}) \mathrm{e}^{-\mathrm{i}\epsilon^{-1}\boldsymbol{l}\cdot\boldsymbol{x}} [W^\epsilon(\boldsymbol{x}, \boldsymbol{k}+\boldsymbol{l}/2) + W^\epsilon(\boldsymbol{x}, \boldsymbol{k}-\boldsymbol{l}/2)] \, \mathrm{d}\boldsymbol{l} \\
&+ i\epsilon^{-1/2} \boldsymbol{k} \cdot \int \hat{\boldsymbol{v}}(\boldsymbol{l}) \mathrm{e}^{-\mathrm{i}\epsilon^{-1}\boldsymbol{l}\cdot\boldsymbol{x}} [W^\epsilon(\boldsymbol{x}, \boldsymbol{k}+\boldsymbol{l}/2) - W^\epsilon(\boldsymbol{x}, \boldsymbol{k}-\boldsymbol{l}/2)] \, \mathrm{d}\boldsymbol{l} \\
&+ \boldsymbol{k} \cdot \nabla_{\boldsymbol{x}} W^\epsilon \\
&+ \mathrm{i}\frac{\epsilon^{-1/2}}{2} \int -|\boldsymbol{l}|^2 \hat{\psi}(\boldsymbol{l}) \mathrm{e}^{-\mathrm{i}\epsilon^{-1}\boldsymbol{l}\cdot\boldsymbol{x}} [W^\epsilon(\boldsymbol{x}, \boldsymbol{k}+\boldsymbol{l}/2) - W^\epsilon(\boldsymbol{x}, \boldsymbol{k}-\boldsymbol{l}/2)] \, \mathrm{d}\boldsymbol{l} = 0,
\end{aligned}
\tag{A5}
$$

where $\hat{\boldsymbol{v}}$ is the Fourier transform of the velocity $\boldsymbol{v}(\boldsymbol{\xi}, t) \equiv \nabla_{\boldsymbol{\xi}}^{\perp} \psi$, i.e.

$$
\hat{\boldsymbol{v}}(\boldsymbol{l}) = \frac{1}{4\pi^2} \int \mathrm{e}^{\mathrm{i}\boldsymbol{l}\cdot\boldsymbol{\xi}} \boldsymbol{v}(\boldsymbol{\xi}, t) \, \mathrm{d}\boldsymbol{\xi},
\tag{A6}
$$

and similarly $\hat{\psi}$ is the Fourier transform of ψ with respect to $\boldsymbol{\xi}$. The dependence of W^ϵ, $\hat{\boldsymbol{v}}$ and $\hat{\psi}$ on time has been omitted for clarity. We stress that the streamfunction, hence the velocity, depend on the slow time variable t, not the fast time t/ϵ associated with the wave frequency. This assumption justifies the expansion (A9) below.

Eq. (A5) can be rewritten as

$$
\begin{aligned}
\partial_t W^\epsilon &+ \boldsymbol{k} \cdot \nabla_{\boldsymbol{x}} W^\epsilon + \epsilon^{-1/2} \mathcal{L}^\epsilon W^\epsilon \\
&+ \frac{\epsilon^{1/2}}{2} \int \hat{\boldsymbol{v}}(\boldsymbol{l}) \mathrm{e}^{-\mathrm{i}\epsilon^{-1}\boldsymbol{l}\cdot\boldsymbol{x}} \cdot \nabla_{\boldsymbol{x}} [W^\epsilon(\boldsymbol{x}, \boldsymbol{k}+\boldsymbol{l}/2) + W^\epsilon(\boldsymbol{x}, \boldsymbol{k}-\boldsymbol{l}/2)] \, \mathrm{d}\boldsymbol{l} = 0,
\end{aligned}
\tag{A7}
$$

where

$$
\mathcal{L}^\epsilon W^\epsilon = \mathrm{i} \int \hat{V}(\boldsymbol{k}, \boldsymbol{l}) \mathrm{e}^{-\mathrm{i}\epsilon^{-1}\boldsymbol{l}\cdot\boldsymbol{x}} [W^\epsilon(\boldsymbol{x}, \boldsymbol{k}+\boldsymbol{l}/2) - W^\epsilon(\boldsymbol{x}, \boldsymbol{k}-\boldsymbol{l}/2)] \, \mathrm{d}\boldsymbol{l}
$$

is the sum of the third and fifth terms of equation (A5). The potential V is defined through its Fourier transform

$$
\hat{V}(\boldsymbol{k}, \boldsymbol{l}) = \boldsymbol{k} \cdot \hat{\boldsymbol{v}}(\boldsymbol{l}) - |\boldsymbol{l}|^2 \hat{\psi}(\boldsymbol{l})/2 = (i\boldsymbol{k} \times \boldsymbol{l} - |\boldsymbol{l}|^2/2) \hat{\psi}(\boldsymbol{l}),
\tag{A8}
$$

with $\boldsymbol{k} \times \boldsymbol{l} = k_1 l_2 - k_2 l_1$ for $\boldsymbol{k} = (k_1, k_2)$ and $\boldsymbol{l} = (l_1, l_2)$. Note that (A7) makes use of the non-divergence of the background flow velocity $\nabla_{\boldsymbol{\xi}} \cdot \boldsymbol{v} = 0$.

3. Asymptotic expansion, random flow and transport equation

We can now derive a transport equation from (A7) using a multiscale approach that treats $\boldsymbol{x}$ and $\boldsymbol{\xi}$ as independent variables,: expanding W^ϵ in powers of $\epsilon^{1/2}$ and assuming that the leading order does not depend on the small scale, we write

$$W^\epsilon(\boldsymbol{x}, \boldsymbol{\xi}, \boldsymbol{k}, t) = W^{(0)}(\boldsymbol{x}, \boldsymbol{k}, t) + \epsilon^{1/2}W^{(1)}(\boldsymbol{x}, \boldsymbol{\xi}, \boldsymbol{k}, t) + \epsilon W^{(2)}(\boldsymbol{x}, \boldsymbol{\xi}, \boldsymbol{k}, t) + O(\epsilon^{3/2}). \quad \text{(A9)}$$

At order $\epsilon^{-1/2}$, we find the same balance as in Ref. 25,

$$\boldsymbol{k} \cdot \boldsymbol{\nabla}_{\boldsymbol{\xi}} W^{(1)} + \theta W^{(1)} = -\mathcal{L}^\epsilon W^{(0)}, \quad \text{(A10)}$$

where θ is a regularization parameter which will be set to zero later. The solution is easily obtained in Fourier space as

$$\hat{W}^{(1)}(\boldsymbol{x}, \boldsymbol{p}, \boldsymbol{k}, t) = \hat{V}(\boldsymbol{k}, \boldsymbol{p})\hat{Y}(\boldsymbol{x}, \boldsymbol{p}, \boldsymbol{k}, t), \quad \text{(A11)}$$

where $\hat{W}^{(1)}$ is the Fourier transform of $W^{(1)}$ with respect to $\boldsymbol{\xi}$ and

$$\hat{Y}(\boldsymbol{x}, \boldsymbol{p}, \boldsymbol{k}, t) = \frac{W^{(0)}(\boldsymbol{x}, \boldsymbol{k} + \boldsymbol{p}/2, t) - W^{(0)}(\boldsymbol{x}, \boldsymbol{k} - \boldsymbol{p}/2, t)}{\boldsymbol{k} \cdot \boldsymbol{p} + \mathrm{i}\theta}. \quad \text{(A12)}$$

At the next order, $O(\epsilon^0)$, we find

$$\partial_t W^{(0)} + \boldsymbol{k} \cdot \boldsymbol{\nabla}_{\boldsymbol{x}} W^{(0)} + \boldsymbol{k} \cdot \boldsymbol{\nabla}_{\boldsymbol{\xi}} W^{(2)} + \mathcal{L}^\epsilon W^{(1)}$$
$$+ \frac{1}{2} \int \mathrm{e}^{-\mathrm{i}\epsilon^{-1}\boldsymbol{l}\cdot\boldsymbol{x}} \hat{\boldsymbol{v}}(\boldsymbol{l}) \cdot \boldsymbol{\nabla}_{\boldsymbol{\xi}}[W^{(1)}(\boldsymbol{x}, \boldsymbol{\xi}, \boldsymbol{k} + \boldsymbol{l}/2, t) + W^{(1)}(\boldsymbol{x}, \boldsymbol{\xi}, \boldsymbol{k} - \boldsymbol{l}/2, t)] \, \mathrm{d}\boldsymbol{l} = 0 \quad \text{(A13)}$$

We now introduce the statistical average $\langle \cdot \rangle$. It can be thought as an ensemble average or, equivalently, as an average over $\boldsymbol{\xi}$. Assuming that the flow is homogeneous, we define the covariance R of the streamfunction as

$$R(\boldsymbol{\xi} - \boldsymbol{\xi}') = \langle \psi(\boldsymbol{\xi})\psi(\boldsymbol{\xi}') \rangle. \quad \text{(A14)}$$

Its Fourier transform with respect to $\boldsymbol{\xi}$, the power spectrum, is related to $\hat{\psi}$ through

$$\langle \hat{\psi}(\boldsymbol{l})\hat{\psi}(\boldsymbol{l}') \rangle = \hat{R}(\boldsymbol{l})\delta(\boldsymbol{l} + \boldsymbol{l}'), \quad \text{(A15)}$$

where δ is the Dirac distribution.

Averaging (A13) and assuming that the small-scale average of the Wigner function is supported by $W^{(0)}$, i.e. $\langle W^\epsilon \rangle = \langle W^{(0)} \rangle$, leads to

$$\partial_t W^{(0)} + \boldsymbol{k} \cdot \boldsymbol{\nabla}_{\boldsymbol{x}} W^{(0)} + \langle \mathcal{L}^\epsilon W^{(1)} \rangle$$
$$+ \langle \frac{1}{2} \int e^{-i\epsilon^{-1}\boldsymbol{l}\cdot\boldsymbol{x}} \hat{\boldsymbol{v}}(\boldsymbol{l}) \cdot \boldsymbol{\nabla}_\xi [W^{(1)}(\boldsymbol{x},\xi,\boldsymbol{k}+\boldsymbol{l}/2,t) + W^{(1)}(\boldsymbol{x},\xi,\boldsymbol{k}-\boldsymbol{l}/2,t)]\,\mathrm{d}\boldsymbol{l} \rangle = 0, \quad (A16)$$

since $\langle \boldsymbol{\nabla}_\xi W^{(2)} \rangle = 0$ and $\langle W^{(0)} \rangle = W^{(0)}$.

Using (A11) and (A12), it can be shown that the last term of (A16) is equal to

$$\frac{1}{2} \iint e^{-i\epsilon^{-1}(\boldsymbol{l}+\boldsymbol{l}')\cdot\boldsymbol{x}} \boldsymbol{l}' \times \boldsymbol{l}\, [i(\boldsymbol{k}+\boldsymbol{l}/2) \times \boldsymbol{l}' - |\boldsymbol{l}'|^2/2] \langle \hat{\psi}(\boldsymbol{l})\hat{\psi}(\boldsymbol{l}') \rangle \hat{Y}(\boldsymbol{x},\boldsymbol{l}',\boldsymbol{k}+\boldsymbol{l}/2,t)\,\mathrm{d}\boldsymbol{l}\mathrm{d}\boldsymbol{l}'$$
$$+ \frac{1}{2} \iint e^{-i\epsilon^{-1}(\boldsymbol{l}+\boldsymbol{l}')\cdot\boldsymbol{x}} \boldsymbol{l}' \times \boldsymbol{l}\, [\mathrm{i}(\boldsymbol{k}-\boldsymbol{l}/2) \times \boldsymbol{l}' - |\boldsymbol{l}'|^2/2] \langle \hat{\psi}(\boldsymbol{l})\hat{\psi}(\boldsymbol{l}') \rangle \hat{Y}(\boldsymbol{x},\boldsymbol{l}',\boldsymbol{k}-\boldsymbol{l}/2,t)\,\mathrm{d}\boldsymbol{l}\mathrm{d}\boldsymbol{l}',$$

which, from (A15), clearly vanishes. Hence the transport equation for $W^{(0)}$ reduces to

$$\partial_t W^{(0)} + \boldsymbol{k} \cdot \boldsymbol{\nabla}_{\boldsymbol{x}} W^{(0)} = \overline{\mathcal{L}^\epsilon} W^{(0)}, \tag{A17}$$

where

$$\overline{\mathcal{L}^\epsilon} W^{(0)} = 4\pi \int [|\boldsymbol{k} \times \boldsymbol{p}|^2 + |\boldsymbol{p}-\boldsymbol{k}|^4/4] \hat{R}(\boldsymbol{p}-\boldsymbol{k})\delta(\boldsymbol{k}^2 - \boldsymbol{p}^2) \left(W^{(0)}(\boldsymbol{x},\boldsymbol{p},t) - W^{(0)}(\boldsymbol{x},\boldsymbol{k},t) \right)\,\mathrm{d}\boldsymbol{p} \tag{A18}$$

is obtained from $\langle \mathcal{L}^\epsilon W^{(1)} \rangle$ in (A16) using (A11), (A12), (A15) and setting $\theta \to 0$ (see Ref. 25). Eq. (A18) involves two terms: the first, proportional to $|\boldsymbol{p}-\boldsymbol{k}|^4/4$ is due to refraction and is the only one present for the Schrödinger equation [25]; the second, proportional to $|\boldsymbol{k} \times \boldsymbol{p}|^2$, appears as a result of advection. The total scattering cross-section is

$$\Sigma = 4\pi \int [(\boldsymbol{k} \times \boldsymbol{p})^2 + |\boldsymbol{p}-\boldsymbol{k}|^4/4] \hat{R}(\boldsymbol{p}-\boldsymbol{k})\delta(\boldsymbol{k}^2 - \boldsymbol{p}^2)\,\mathrm{d}\boldsymbol{p}.$$

Note that (7) is the dimensional version of (A17).

Appendix B: Eigenvalues of $\mathcal{L}$ for $|\boldsymbol{k}| \gg k_\mathrm{c}$

We approximate the eigenvalues λ_n (see (19)) for $|\boldsymbol{k}| \gg k_\mathrm{c}$. Because $\sigma'(|\boldsymbol{k}|,\theta) = \sigma'(|\boldsymbol{k}|,-\theta)$, λ_n is equal to

$$\lambda_n = \frac{8\pi|\boldsymbol{k}|^4 A}{h} \int_{-\pi}^{\pi} \sin^2(\theta/2) \exp(-\gamma \sin^2(\theta/2) + in\theta)\,\mathrm{d}\theta, \tag{B1}$$

where $\gamma = 2|\boldsymbol{k}|^2/k_\mathrm{c}^2$ and we have used $\hat{R}(|\boldsymbol{p}|) = A \exp(-|\boldsymbol{p}|^2/(2k_\mathrm{c}^2))$ in (B1). We describe in B 1 the steepest-descent method used to approximate (B1) for finite n/γ; an approximation for small n is derived in B 2 by Laplace's method.

31

1. Uniform approximation

We derive an approximation valid uniformly for $n = O(1)$ and $n = O(\gamma) \gg 1$ by writing $n = \gamma m$. Eq. (B1) then becomes

$$\lambda_n = \frac{16\pi|\boldsymbol{k}|^4 A}{h} \int_{-\pi/2}^{\pi/2} \sin^2\theta \exp(-\gamma g(\theta))\, d\theta, \tag{B2}$$

where $g(\theta) = \sin^2\theta - 2im\theta$. Because $\gamma \gg 1$ in the regime considered here, the integral is dominated by the contribution of the integrand at the critical points of $g(\theta)$, and a steepest-descent method may be applied. Solving $g'(\theta) = 0$ gives one single critical point

$$\theta^* = i/2\sinh^{-1}(2m) \in i\mathbb{R}. \tag{B3}$$

Because $g''(\theta^*) = 2\cos(2\theta^*) > 0$, one can change the path of integration in (B2) from the real-axis segment $[-\pi/2, \pi/2]$ to a curve $\mathcal{C}$ in the complex plan with the same end points and passing through θ^*, where it crosses the imaginary axis orthogonally. Eq. (B2) then becomes approximately

$$\lambda_n \simeq \frac{16\pi|\boldsymbol{k}|^4 A}{h} \exp(-\gamma g(\theta^*)) \int_{\mathcal{C}} d\theta \sin^2\theta$$
$$\times \exp\left(-\gamma\frac{g''(\theta^*)}{2}(\theta-\theta^*)^2 - \gamma\frac{g^{(3)}(\theta^*)}{6}(\theta-\theta^*)^3 - \gamma\frac{g^{(4)}(\theta^*)}{24}(\theta-\theta^*)^4\right). \tag{B4}$$

It is important to keep all orders in the exponential up to $(\theta-\theta^*)^4$ in order to calculate the first-order correction to λ_n. Introducing the Taylor expansion

$$\sin^2\theta \simeq \sin^2\theta^* + \sin(2\theta^*)(\theta-\theta^*) + \cos(2\theta^*)(\theta-\theta^*)^2 - \frac{2}{3}\sin(2\theta^*)(\theta-\theta^*)^3 - \frac{1}{3}\cos(2\theta^*)(\theta-\theta^*)^4 \tag{B5}$$

into the integral (B4) and Taylor-expanding the exponential gives

$$\lambda_n \simeq \frac{16\pi|\boldsymbol{k}|^4 A}{h} \exp(-\gamma g(\theta^*)) \times$$
$$\left(\sin^2\theta^* \int_{\mathcal{C}} \exp(-\gamma\frac{g''(\theta^*)}{2}(\theta-\theta^*)^2)\, d\theta\right.$$
$$+ \cos(2\theta^*) \int_{\mathcal{C}} (\theta-\theta^*)^2 \exp(-\gamma\frac{g''(\theta^*)}{2}(\theta-\theta^*)^2)\, d\theta$$
$$- \gamma\left(\sin(2\theta^*)\frac{g^{(3)}(\theta^*)}{6} + \sin^2\theta^*\frac{g^{(4)}(\theta^*)}{24}\right) \int_{\mathcal{C}} (\theta-\theta^*)^4 \exp(-\gamma\frac{g''(\theta^*)}{2}(\theta-\theta^*)^2)\, d\theta$$
$$\left.+ \gamma^2 \sin^2\theta^* \frac{(g^{(3)}(\theta^*))^2}{72} \int_{\mathcal{C}} (\theta-\theta^*)^6 \exp(-\gamma\frac{g''(\theta^*)}{2}(\theta-\theta^*)^2)\, d\theta\right). \tag{B6}$$

32

Note that we have discarded some terms in (B6) because they appear at a higher order in γ^{-1}. Moreover we have used symmetry properties to eliminate some integrals. The integrals appearing in (B6) are standard and we obtain, for large γ,

$$
\begin{aligned}
\lambda_n \simeq \frac{16\pi|\boldsymbol{k}|^4 A}{h} \exp(-\gamma g(\theta^*)) \times \bigg(& \sin^2\theta^* \sqrt{\frac{2\pi}{g''(\theta^*)}} \gamma^{-1/2} + \cos(2\theta^*) \frac{\sqrt{2\pi}}{g''(\theta^*)^{3/2}} \gamma^{-3/2} \\
& - \left(\sin(2\theta^*) \frac{g^{(3)}(\theta^*)}{6} + \sin^2\theta^* \frac{g^{(4)}(\theta^*)}{24} \right) \frac{3\sqrt{2\pi}}{g''(\theta^*)^{5/2}} \gamma^{-3/2} + \sin^2\theta^* \frac{15\sqrt{2\pi}(g^{(3)}(\theta^*))^2}{72 g''(\theta^*)^{7/2}} \gamma^{-3/2} \bigg).
\end{aligned}
\tag{B7}
$$

The presence of the last two terms in (B7), at the same order as the second term (proportional to $\cos(2\theta^*)$), justifies a posteriori the Taylor expansion of $g(\theta)$ near θ^* in the exponential in (B4). Finally, using the value of θ^* (B3) and some trigonometric identities yields (31).

2. Approximation for small n/γ

Eq. (B1) can be rewritten as

$$
\lambda_n = \frac{16\pi|\boldsymbol{k}|^4 A}{h} \int_{-\pi/2}^{\pi/2} \cos(2n\theta) \sin^2\theta \exp(-\gamma \sin^2\theta) \, d\theta,
\tag{B8}
$$

For large γ, this integral is dominated by the contribution of the integrand near $\theta = 0$. Therefore, we Taylor-expand there the various terms to obtain

$$
\lambda_n \simeq \frac{16\pi|\boldsymbol{k}|^4 A}{h} \int_{-\pi/2}^{\pi/2} (1 - 2n^2\theta^2)(\theta^2 - \theta^4/3)(1 + \gamma\theta^4/3) \exp(-\gamma\theta^2) \, d\theta.
\tag{B9}
$$

Re-arranging terms this becomes

$$
\lambda_n \simeq \frac{16\pi|\boldsymbol{k}|^4 A}{h} \int_{-\pi/2}^{\pi/2} \left(1 - (2n^2 + 1/3)\theta^2 + \gamma\theta^4/3\right) \theta^2 \exp(-\gamma\theta^2) \, d\theta,
\tag{B10}
$$

and, on integrating,

$$
\lambda_n \simeq \frac{8\pi^{3/2}|\boldsymbol{k}|^4 A}{h} \gamma^{-3/2} \left(1 + \gamma^{-1}(3/4 - 3n^2)\right),
\tag{B11}
$$

which yields (32).

---

[1] M. H. Alford, J. A. MacKinnon, H. L. Simmons, and J. D. Nash, "Near-inertial internal gravity waves in the ocean," Annu. Rev. Mar. Sci. **8**, 95–123 (2016).

[2] W. Blumen, "Geostrophic adjustment," Rev. Geophys. Space Phys. **10**, 485–528 (1972).

[3] A. E. Gill, "Atmosphere ocean dynamics," Academic Press, New York , 662pp (1982).

[4] F. Lott, "Large-scale flow response to short gravity waves breaking in a rotating shear flow," J. Atmos. Sc. **60**, 1691–1704 (2003).

[5] M. Nikurashin and R. Ferrari, "Radiation and dissipation of internal waves generated by geostrophic motions impinging on small-scale topography: Theory," J. Phys. Oceanogr. **40**, 1055–1074 (2010).

[6] E. Danioux, J. Vanneste, P. Klein, and H. Sasaki, "Spontaneous inertia-gravity-wave generation by surface-intensified turbulence," J. Fluid Mech. **699**, 153–173 (2012).

[7] M. H. Alford, A. Y. Shcherbina, and M. C. Gregg, "Observations of near-inertial internal gravity waves radiating from a frontal jet," J. Phys. Oceanogr. **43**, 1225–1239 (2013).

[8] Shuwen Zhang, Lingling Xie, Yijun Hou, Hui Zhao, Yiquan Qi, and Xiaofei Yi, "Tropical storm-induced turbulent mixing and chlorophyll-a enhancement in the continental shelf southeast of hainan island," J. Mar. Res. **129**, 405–414 (2014).

[9] M. H. Alford, M. F. Cronin, and J. M. Klymak, "Annual cycle and depth penetration of wind-generated near-inertial internal waves at ocean station papa in the northeast pacific," J. Phys. Oceanogr. **42**, 889–909 (2012).

[10] N. Furuichi, T. Hibiya, and Y. Niwa, "Model-predicted distribution of wind-induced internal wave energy in the world's oceans," J. Geophys. Res. **113**, C09034 (2008).

[11] D. B. Whitt and L. N. Thomas, "Near-inertial waves in strongly baroclinic currents," J. Phys. Oceanogr. **43**, 706–725 (2013).

[12] D. B. Whitt and L. N. Thomas, "Resonant generation and energetics of wind-forced near-inertial motions in a geostrophic flow," J. Phys. Oceanogr. **45**, 181–208 (2015).

[13] J.-H. Xie and J. Vanneste, "A generalised-Lagrangian-mean model of the interactions between near-inertial waves and mean flow," J. Fluid Mech. **774**, 143–169 (2015).

[14] Xiaoming Zhai, R. J. Greatbach, and Jun Zhao, "Enhanced vertical propagation of storm-induced near-inertial energy in an eddying ocean channel model," Geophys. Res. Lett. **32**, L18602 (2005).

[15] C. N. K. Mooers, "Several effects of a baroclinic current on the cross-stream propagation of inertial-internal waves," Geophys. Fluid. Dyn. **6**, 245–275 (1975).

[16] C. N. K. Mooers, "Several effects of baroclinic currents on the three-dimensional propagation of inertial-internal waves," Geophys. Fluid. Dyn. **6**, 277–284 (1975).

[17] D. J. Olbers, "The propagation of internal waves in a geostrophic current," J. Phys. Oceanogr. **11**, 1224–1233 (1981).

[18] E. Kunze, "Near-inertial wave propagation in geostrophic shear," J. Phys. Oceanogr. **15**, 544–565 (1985).

[19] W. R. Young and M. Ben Jelloul, "Propagation of near-inertial oscillations through a geostrophic flow," J. Mar. Res. **55**, 735–766 (1997).

[20] P. Klein, S. Llewellyn Smith, and G. Lapeyre, "Spatial organisation of inertial energy by an eddy field," Q. J. R. Meteorol. Soc. **130**, 1153–1166 (2004).

[21] E. Danioux, P. Klein, and P. Rivière, "Propagation of wind energy into the deep ocean through a fully turbulent mesoscale eddy field," J. Phys. Oceanogr. **38**, 2224–2241 (2008).

[22] E. A. D'Asaro, "The energy flux from the wind to near-inertial motions in the surface mixed layer," J. Phys. Oceanogr. **15**, 1043–1059 (1985).

[23] M. H. Alford, "Improved global maps and 54-year history of wind-work on ocean inertial motions," Geophys. Res. Lett. **30(8)**, 1424:doi,10.1029/2002GL016614 (2003).

[24] K. E. Silverthorne and J. M. Toole, "Seasonal kinetic energy variability of near-inertial motions," J. Phys. Oceanogr. **39**, 1035–1049 (2009).

[25] L. Ryzhik, G. Papanicolaou, and J. B. Keller, "Transport equations for elastic and other waves in random media," Wave Motion , 327–370 (1996).

[26] J. M. Powell and J. Vanneste, "Transport equations for waves in randomly perturbed hamiltonian systems, with application to rossby waves," Wave Motion **42**, 289–308 (2005).

[27] E. Danioux, J. Vanneste, and O. Bühler, "Concentration of near-inertial waves in anticyclones: an energetic argument," J. Fluid Mech. **773**, R2 (2015).

[28] N. J. Balmforth, S.G. Llewellyn Smith, and W. R. Young, "Enhanced dispersion of near-inertial waves in an idealized geostrophic flow," J. Mar. Res. **56**, 1–40 (1998).

[29] The correlation length ℓ_c is defined as $\ell_c = 2\pi/K_c$, where $K_c = \iint |\boldsymbol{k}| \hat{R}(\boldsymbol{k}) \, \mathrm{d}\boldsymbol{k} / \iint \hat{R}(\boldsymbol{k}) \, \mathrm{d}\boldsymbol{k}$ is the correlation wavenumber.

[30] N. Komori, W. Ohfuchi, B. Taguchi, H. Sasaki, and P. Klein, "Deep ocean inertia-gravity waves simulated in a high-resolution global coupled atmosphere/ocean GCM," Geophys. Res. Lett. **35**, L04610 (2008).

[31] A. T. Blaker, J. J.-M. Hirschi, B. Sinha, B. de Cuevas, S. Alderson, A. Coward, and G. Madec, "Large near-inertial oscillations of the atlantic meridional overturning circulation ocean modelling," Ocean Modell. **42**, 50–56 (2012).

[32] E. A. D'Asaro, C. C. Eriksen, M. D. Levine, C. A. Paulson, P. Niiler, and P. Van Meurs, "Upper-ocean inertial currents forced by a strong storm. Part I: Data and comparisons with linear theory," J. Phys. Oceanogr. **25**, 2909–2936 (1995).

[33] O. Bühler, "Equatorward propagation of inertia–gravity waves due to steady and intermittent wave sources," J. Atmos. Sci. **60**, 1410–1419 (2003).

[34] P. Y. Le Traon, P. Klein, Bach Lien Hua, and G. Dibarboure, "Do altimeter wavenumber spectra agree with the interior or surface quasigeostrophic theory?" J. Phys. Oceanogr. **38(5)**, 1137–1142 (2008).

[35] J. E. Geisler, "Linear theory of the response of a two layer ocean to a moving hurricane," Geophys. Fluid Dyn. **1**, 249–272 (1970).

[36] J. Nilsson, "Energy flux from traveling hurricanes to the oceanic internal wave field," J. Phys. Oceanogr. **25**, 558–573 (1995).

[37] V. Zervakis and M. D. Levine, "Near-inertial energy propagation from the mixed layer: Theoretical considerations," J. Phys. Oceanogr. **25**, 2872–2889 (1995).

[38] S. W. Chang and R. A. Anthes, "Numerical simulations of the ocean's nonlinear, baroclinic response to translating hurricanes," J. Phys. Oceanogr. **8**, 468–480 (1978).

[39] R. J. Greatbatch, "On the response of the ocean to a moving storm: The nonlinear dynamics," J. Phys. Oceanogr. **13**, 357–367 (1983).

[40] R. J. Greatbatch, "On the response of the ocean to a moving storm: Parameters and scales," J. Phys. Oceanogr. **14**, 59–78 (1984).

[41] J. F. Price, T. B. Sanford, and G. Z. Forristall, "Forced stage response to a moving hurricane," J. Phys. Oceanogr. **24**, 233–260 (1994).

[42] Y. Niwa and T. Hibiya, "Nonlinear processes of energy transfer from traveling hurricanes to the deep ocean internal wave field," J. Geophys. Res. **102 (C6)**, 12,469–12,477 (1997).

[43] S. E. Zedler, "The simulated ocean response to a hurricane. nonlinear processes," J. Phys. Oceanogr. **39**, 2618–2634 (2009).

[44] J. F. Price, "Internal wave wake of a moving storm. Part I. Scales, energy, budget and observation," J. Phys. Oceanogr. **13**, 949–965 (1983).

[45] M.-P. Lelong and J. J. Riley, "Internal wave-vortical mode interactions in strongly stratified flows," J. Fluid Mech. **232**, 1–19 (1991).

[46] P. Bartello, "Geostrophic adjustment and inverse cascades in rotating stratified turbulence," J. Atmos. Sc. **52**, 4410–4428 (1995).

[47] M. Ward and W. K. Dewar, "Scattering of gravity waves by potential vorticity in a shallow-water fluid," J. Fluid Mech. **663**, 478–506 (2010).

[48] P. Müller and N. Xu, "Scattering of oceanic internal gravity waves off random bottom topography," J. Phys. Oceanogr. **22**, 474–488 (1992).

[49] A. L. Ponte and P. Klein, "Incoherent signature of internal tides on sea level in idealized numerical simulations," Geophys. Res. Lett. **42**, 1520–1526 (2015).